SPECIAL
GDIS Drought Worldwide
COLLECTION

∂Regional Model Simulations of the 2008 Drought in Southern South America Using a Consistent Set of Land Surface Properties

Omar V. Müller

CEVARCAM, Facultad de Ingeniería y Ciencias Hídricas, Universidad Nacional del Litoral and CONICET, Santa Fe, Argentina

Ernesto Hugo Berbery

Cooperative Institute for Climate and Satellites-Maryland, Earth System Science Interdisciplinary Center, University of Maryland, College Park, College Park, Maryland

Domingo Alcaraz-Segura

Departamento de Botánica, Campus de Fuente Nueva, Universidad de Granada, Granada, Spain

Michael B. Ek

Environmental Modeling Center, NOAA/NCEP/NWS, College Park, Maryland

ABSTRACT

This work discusses the land surface–atmosphere interactions during the severe drought of 2008 in southern South America, which was among the most severe in the last 50 years in terms of both intensity and extent. Once precipitation returned to normal values, it took about two months for the soil moisture content and vegetation to recover. The land surface effects were examined by contrasting long-term simulations using a consistent set of satellite-derived annually varying land surface biophysical properties against simulations using the conventional land-cover types in the Weather Research and Forecasting Model–Noah land surface model (WRF–Noah). The new land-cover dataset is based on ecosystem functional properties that capture changes in vegetation status due to climate anomalies and land-use changes.

The results show that the use of realistic information of vegetation states enhances the model performance, reducing the precipitation biases over the drought region and over areas of excessive precipitation. The precipitation bias reductions are attributed to the corresponding changes in greenness fraction, leaf area index, stomatal resistance, and surface roughness. The temperature simulation shows a generalized increase, which is attributable to a lower vegetation greenness and a doubling of the stomatal resistance that reduces the evapotranspiration rate. The increase of temperature has a beneficial effect toward the eastern part of the domain with a notable reduction of the bias, but not over the central region where the bias is increased. The overall results suggest that an improved representation of the surface processes may contribute to improving the predictive skill of the model system.

1. Introduction

Land surface processes are recognized as a potential source of climate variability and predictability at different time scales, from hours to seasons and longer

Corresponding author address: Omar V. Müller, CEVARCAM, FICH, UNL, Ciudad Universitaria, Santa Fe 3000, Argentina.
E-mail: ovmuller@unl.edu.ar

(Koster et al. 2000; Koster and Suarez 2003; Guo et al. 2011; Sellers et al. 1992; Foley et al. 2000). Changes in the land surface or vegetation cover can affect the way the land and the atmosphere interact at many of those time scales and can thus have an effect on climate. Changes in the surface states result from land-use and land-cover changes, either from natural or anthropogenic origin or from climate conditions that affect the vegetation health and its phenology. Abundant evidence based on model simulations has been offered on the impacts of land-cover changes on regional to global climate and will not be reviewed here

(see, e.g., Pielke et al. 2007, and references therein; Mahmood et al. 2010).

The need for a correct representation of the land surface in models has been discussed for many years (Betts et al. 1996; Ge et al. 2007), and several efforts have been reported with positive results in general. In the most elaborate approach, climate models are being coupled to highly complex dynamical vegetation models with explicit representation of physiological and biogeochemical processes (e.g., Smith et al. 2001; Levis et al. 2004). In most cases, the issue is handled by more empirical approaches. Kurkowski et al. (2003) and Jiang et al. (2010) have found that the use of near-real-time fractional vegetation coverage derived from satellite data in weather model simulations tends to reduce both the near-surface temperature and dewpoint biases. Likewise, the use of realistic leaf area index (LAI) translates into increases of potential predictability of evaporation in tropical and forested areas, although the impact on potential predictability of near-surface temperature is smaller and in some places even negative (Weiss et al. 2012). Tian et al. (2004a,b) indicated that a better representation of vegetation leads to a more realistic surface albedo, of which impacts on climate are well documented. Their results also show that new estimates of LAI, plant functional types, and fractional vegetation cover from the Moderate Resolution Imaging Spectroradiometer (MODIS) continuous vegetation improve the absorption and partitioning of energy between canopy and soil, reducing the model biases.

Numerical experiments using new land surface parameters based on MODIS data show that, for example, the Community Climate System Model (CCSM) is sensitive to the changes in land surface; however, while there are improvements in the simulation of precipitation and near-surface temperature, large biases still remain (Lawrence and Chase 2007). These mixed results are not uncommon in studies of vegetation–atmosphere feedbacks and are a demonstration of the complexity of representing realistically the land surface in climate models. Despite the overall evidence indicating that a more realistic representation of surface conditions reduces model biases, many current numerical models, particularly those used for operational forecasts, still employ fixed land-cover types. Hence, they are unable to represent the additional sources of interannual variability owing to land-cover changes, as a result of either land-use changes or the vegetation's degree of stress (e.g., during droughts, wet periods, or insect outbreaks). In other words, models that do not include changes in land cover may have a limited representation of the land surface–atmosphere feedbacks and consequently on their effects on the regional climate.

South America is a region where climate models tend to have difficulties to properly reproduce the patterns and magnitude of precipitation (e.g., Silvestri and Vera 2008; Solman et al. 2008; Rusticucci et al. 2010). The reasons are not fully understood, but contributing factors are assumed to be the misrepresentation of the actual land-cover types and the consequent inadequate simulation of the land–atmosphere interactions. Vast areas are suffering from human-induced changes in land cover, with deforestation and land clearing for agriculture and cattle ranching being the most important ones (Dros 2004; Paruelo et al. 2005).

This study explores the use of a consistent set of annually varying biophysical properties of vegetation derived from satellite data as a replacement of the conventional land-cover types for southern South America in the Weather Research and Forecasting (WRF) Model coupled with the Noah land surface model (LSM). The new set, named ecosystem functional types (EFTs), takes into account the functional properties of terrestrial ecosystems, as identified using a top-down approach of MODIS measurements of vegetation greenness. This article reports how the newly defined land representation impacts the land–atmosphere interactions and model performance during an intense drought episode that occurred in 2008 in southern South America. The characteristics of the severe drought event are discussed in section 2. Section 3 presents the model configuration and an evaluation of the control simulations. Section 4 introduces the new time-varying but consistent land surface dataset and discusses its biophysical properties and the differences with the traditional land-cover representation. The results of the simulations with the novel dataset, its comparison to the control simulations, and possible mechanisms for the changes are discussed in section 5. A summary discussion is presented in section 6, while the conclusions are offered in section 7.

2. The observed 2008 drought in southern South America

The hypothesis of this research is that a realistic representation of the land-cover properties helps improve the simulation of the land surface–atmosphere interactions and hence can reduce model biases inherent to surface processes. Consequently, it is expected that the effects will be more noticeable during a situation when the surface states depart noticeably from their predefined properties, as during a drought period. For this reason we test our hypothesis for a drought event that took place in southern South America, a region where climate has great economic and social impacts. Other regions within the model domain had excess of precipitation, giving the opportunity to

examine the land–atmosphere interactions and surface effects during very different conditions.

a. Large-scale patterns associated with extremes in southern South America

Southeastern South America has experienced a positive trend in annual precipitation during the second half of the twentieth century (e.g., Krepper and Zucarelli 2009; Doyle et al. 2012). Since Argentina and Uruguay are countries whose economy relies mostly on rain-fed agriculture, the trend has favored the expansion of the agricultural frontier, increasing the availability of productive lands. However, this increase has been accompanied by greater interannual variability in precipitation, which increases the risk not only of flood events but also of droughts with their consequent negative impacts (Penalba et al. 2010).

Extreme events in southern South America recognize as the main driver the Pacific Ocean SST anomalies, especially owing to the ENSO phenomenon (Ropelewski and Halpert 1987; Aceituno 1988; Mechoso and Perez-Iribarren 1992). Positive SST anomalies over the tropical Pacific (El Niño) are known to induce wet spells over southern South America; conversely, a cold tropical Pacific (La Niña) favors dry conditions. The effect of the Pacific Ocean anomalies is enhanced by the north tropical Atlantic when they are in opposite phases. For example, a cold Pacific (La Niña) complemented with a warm north tropical Atlantic induces a distinct drought pattern with a noticeable increase in anomaly strength (Seager et al. 2010; Mo and Berbery 2011).

Much of the work on land-cover changes carried out for South America is focused on the tropical and subtropical regions, but little is found on land surface effects for southern South America. Nevertheless, Lee and Berbery (2012) showed that the regional climate over the La Plata basin is sensitive to idealized changes in land cover. Entekhabi et al. (1992) argued that land surface memory due to soil moisture storage could result in enhancing and prolonging both floods and droughts. Along this reasoning, Hong and Kalnay (2002) showed that, while the 1998 Oklahoma–Texas drought did not originate from surface effects, once it was established, the dry soil anomalies helped to maintain the pattern for several months before the mechanism was overwhelmed by synoptic-scale disturbances in the autumn. Land-cover changes have also been found to affect the character of climate extremes: in eastern Australia, land-cover changes led to an increased number of dry days and a decrease in daily rainfall (Deo et al. 2009).

b. Observations

Two observational precipitation datasets are used to describe the characteristics of the 2008 drought and to evaluate the model performance. They are the National Centers for Environmental Prediction (NCEP) Climate Prediction Center (CPC) global land-only gridded daily precipitation analysis at a 1° × 1° grid spacing derived from gauge-only observations (Shi et al. 2000; Silva et al. 2007) and the Tropical Rainfall Measurement Mission (TRMM) 3B43 monthly satellite data at 0.25° × 0.25° grid spacing (Huffman et al. 2007). We will refer to these two precipitation products as observed and satellite derived, respectively.

Additional variables are employed to assess the land surface conditions during the drought: CPC has created a land-only monthly global surface air temperature dataset based on observations interpolated to a 0.5° × 0.5° grid (Fan and Van den Dool 2008). Also, observed temperature data were collected from 184 gauge stations. CPC is also producing a global soil moisture dataset at 0.5° × 0.5° grid spacing that is computed with a simple water balance model using precipitation and temperature over land as input (Fan and Van den Dool 2004). The CPC soil moisture is used here as an additional indicator of the observed drought, but not for model evaluation as values are highly dependent on model characteristics, preventing a direct comparison between models.

Finally, the normalized difference vegetation index (NDVI) was used to identify ecosystem functional types to capture the seasonal and interannual variability of vegetation primary production. The NDVI dataset was derived from the MODIS vegetation product MOD13C2 for 2001–09. This dataset consists of 16-day maximum value composite global images at a spatial resolution of 0.05° × 0.05°.

c. Observed features of the 2008 drought

The large-scale ocean patterns during the severe drought of 2008 affecting southern South America were consistent with the modes described in section 2a: that is, the combination of a La Niña episode with large tropical North Atlantic warm SST anomalies (not shown). The drought had exceptional characteristics in terms of spatial extension and persistence, causing great economic losses. Bidegain (2009) reported that the spatial extent of the 2008 drought was comparable to or larger than other important droughts in the region that occurred during the last five decades. In several locations, the drought duration was the longest on record, achieving very low values of the standardized precipitation index (SPI), which in some cases became the series absolute minimum (M. Skansi 2009, personal communication).

The spatial distribution of the drought as represented by the precipitation anomalies is shown in Figs. 1a,b. The satellite-derived precipitation anomaly pattern
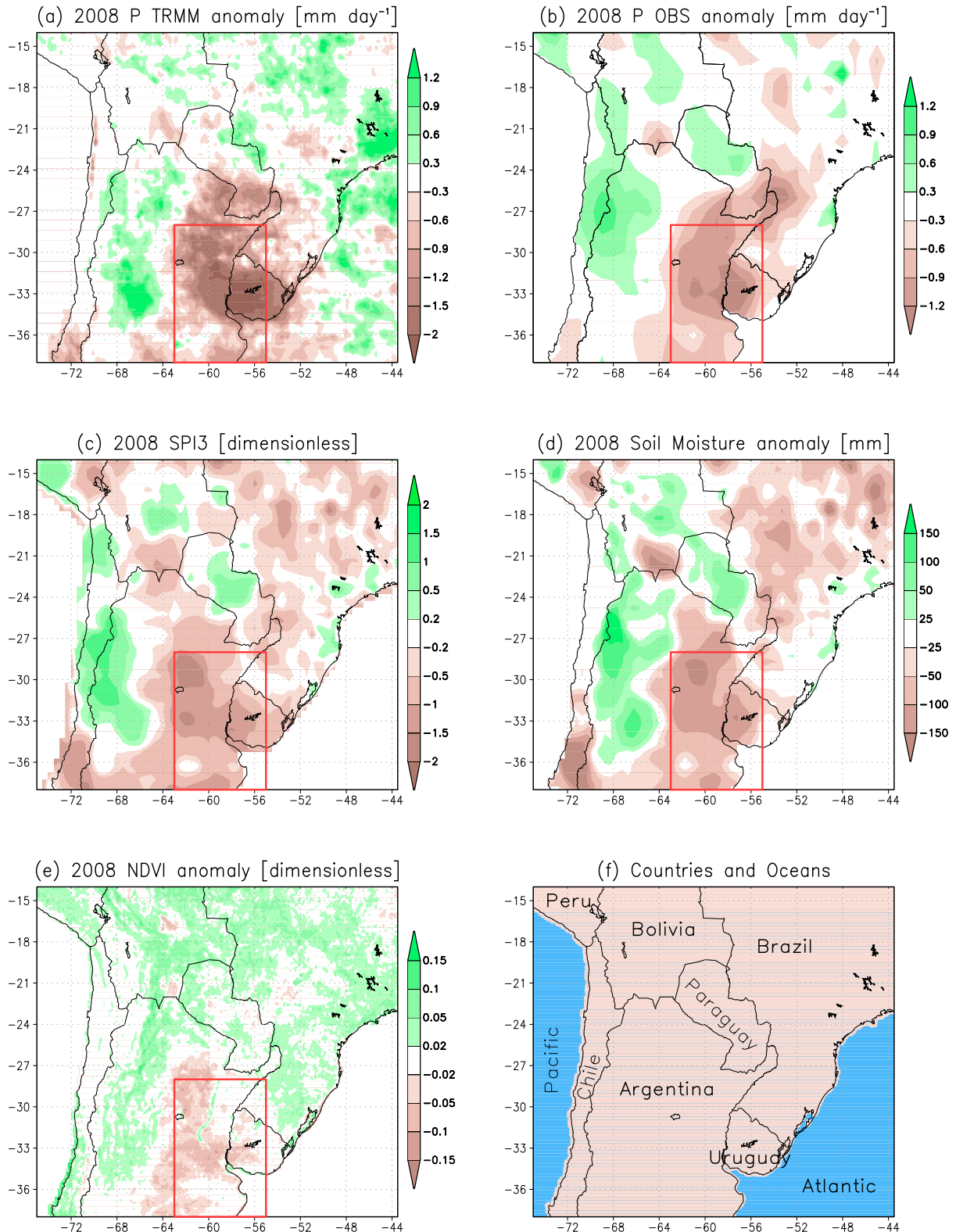
FIG. 1. Year 2008 (a) TRMM precipitation anomalies compared to the average for 1998–2007; (b) observed precipitation anomalies compared to the average for 1979–2007; (c) mean SPI3; (d) CPC soil moisture anomalies compared to the average for 1948–2007; (e) NDVI compared to the average for 1982–2007; and (f) countries and oceans included in the region of interest. The red boxes highlight the main drought area.

(Fig. 1a) shows a negative center over Uruguay, extending over northeastern Argentina and southern Paraguay with a maximum deficit of $2\,\mathrm{mm\,day}^{-1}$ over Uruguay (around 40% of the 1998–2007 mean). The observed rainfall anomalies (Fig. 1b) have a similar pattern, but with a second center over the northeastern tip of Argentina near the border with Brazil and Paraguay (usually known as the tripartite border). The magnitude of the observed anomalies is smaller than those from satellite-derived information, which may be due to the sparsely distributed rain gauges that tend to smooth the rainfall pattern. Figure 1c depicts the 3-month standard precipitation index (SPI3) averaged for 2008. The SPI values (see Mo 2008) identify the main drought area as moderately to severely dry ($-2.0 <$ SPI3 < -1.0). The index also shows the second core, defining it as mildly to moderately dry ($-1.5 <$ SPI3 $<$ 0.0). The rainfall-deficit conditions have an evident effect on the soil moisture availability in northeastern Argentina and most of Uruguay (Fig. 1d). As a consequence of the depletion of rainfall and the reduced soil moisture content, the NDVI anomaly pattern (Fig. 1e) exhibits negative values corresponding to lower vegetation greenness.

Figure 2 presents the evolution of the drought as characterized by an area average over the box 38°–28°S, 63°–55°W. Figures 2a,b indicate that the region first had a rainfall deficit during the austral winter 2007 that recovered during austral spring, only to return to an almost continuous deficit from November 2007 to June 2009. The time series of SPI3 in Fig. 2c repeats the precipitation evolution, showing four local minima classifiable as moderately dry (SPI3 ≈ -1.5). The minimum in August 2007 derives from the first rainfall deficit, and the remaining minima appear lagging one month with respect to the minimum peaks of rainfall, as a consequence of the computation method for SPI3 (Mo 2008). The near-surface temperature in Fig. 2d shows a slight warming of about 0.5°C on average from the mean annual cycle during the longest period of the drought. The soil moisture also follows the rainfall evolution (Fig. 2e), with negative anomalies starting in December 2007 and increasing continuously in magnitude until reaching the largest deficit during the first half of 2009. With the rain returning to normal around July–August 2009, the soil moisture content begins to recover starting in September (austral spring) and returns to climatological values by the end of 2009. The water deficit had a direct effect on NDVI that presents a long period of low vegetation greenness (Fig. 2f) starting about 3 months after the first negative anomalies of precipitation. The time series show that the long-term anomalous precipitation strongly affected vegetation and soil conditions,

which need about 2 months of normal to high precipitation to recover back to their typical mean values.

3. Model configuration and evaluation

a. Model configuration

Numerical simulations of the 2008 drought were carried out with the Advanced Research WRF (ARW), version 3.2, released on 2 April 2010. A full technical description of the system is given in Skamarock et al. (2008). WRF solves the fully compressible nonhydrostatic Eulerian equations in flux form, using a terrain-following hydrostatic pressure vertical coordinate. It is coupled with the Noah LSM version 3.2 that solves the surface energy and water balances to provide sensible and latent heat fluxes to the boundary layer (see Chen et al. 1996; Chen and Dudhia 2001; Ek et al. 2003). The Noah LSM has four soil layers with a corresponding thickness from the top down of 10, 30, 60, and 100 cm (2-m total depth) and includes representations of the root zone, vegetation categories, monthly vegetation fraction, and soil texture. Output variables from the Noah model include evapotranspiration, runoff, soil drainage, soil temperature, and soil moisture content.

The Noah LSM employs a fixed land-use/land-cover map (Anderson et al. 1976), generated by the U.S. Geological Survey (USGS) Center for Earth Resources Observation and Science, the University of Nebraska–Lincoln, and the Joint Research Centre of the European Commission. The map was derived from the National Oceanic and Atmospheric Administration (NOAA) Advanced Very High Resolution Radiometer (AVHRR) images collected daily over a 12-month period from April 1992 through March 1993 with 1-km resolution (Eidenshink and Faudeen 1994). In the case of southern South America, the 1992/93 period was characterized by normal rainfall in most of the domain (not shown), with positive anomalies up to $1.8\,\mathrm{mm\,day}^{-1}$ in northern Bolivia and up to $1\,\mathrm{mm\,day}^{-1}$ in areas of southern Brazil (around 24°S, 52°W).

The WRF–Noah was run with a horizontal grid spacing of 18 km and 28 vertical levels over a domain that covers the southern part of South America (see Fig. 3). It includes the area of the La Plata basin (in red), with significant topographic features like the Andes cordillera toward the west and the Brazilian highlands toward the northeast. Lowlands and plains complete the domain. The model physics configuration follows the selection of schemes and options of Lee and Berbery (2012, see their Table 1) and Lee (2010), who evaluated the combination of parameters that represent the South America climate with smaller biases finding that the
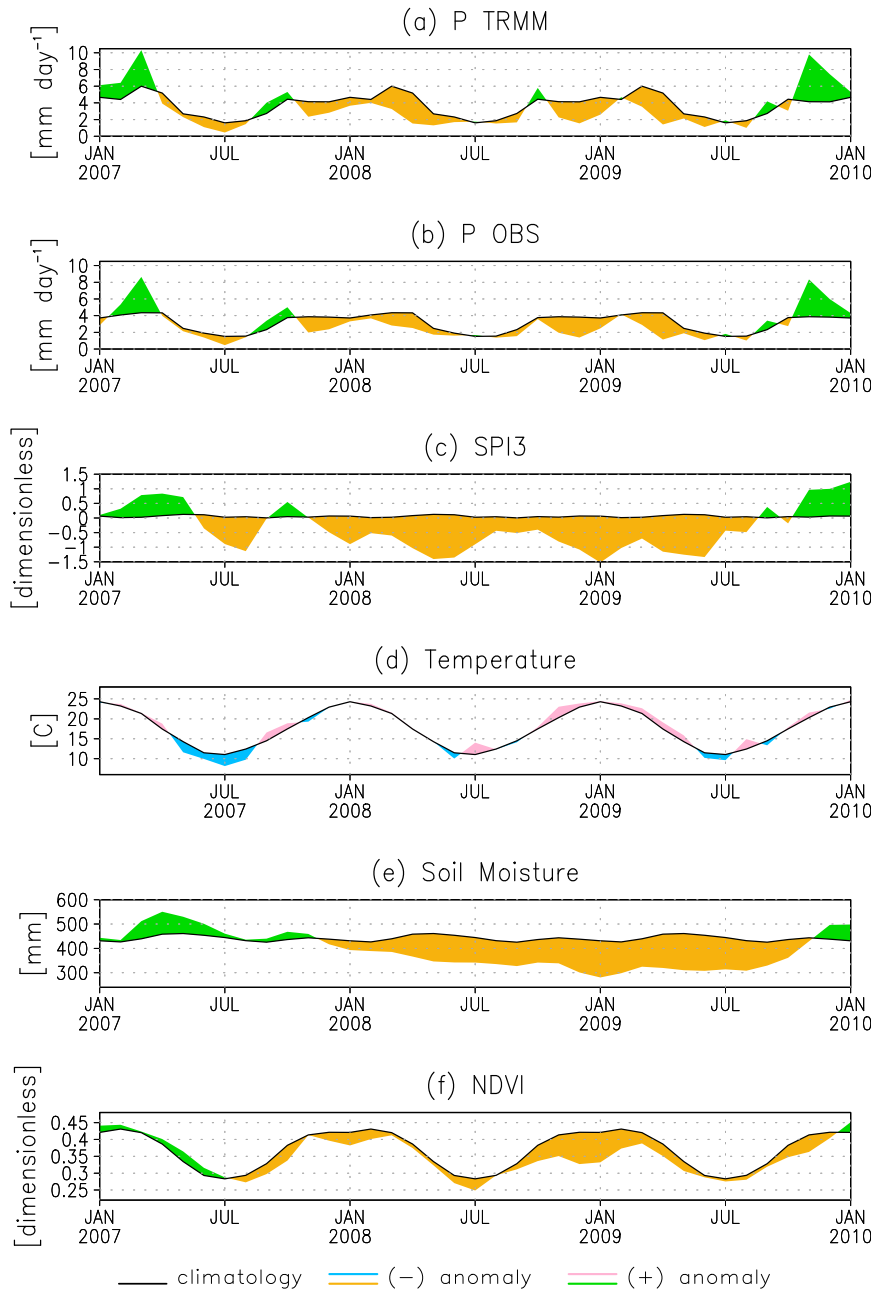
FIG. 2. Land-only area-averaged time series for the drought region (38°–28°S, 63°–55°W) of (a) TRMM precipitation anomalies, (b) observed precipitation anomalies, (c) 3-month SPI, (d) temperature anomalies, (e) soil moisture anomalies, and (f) NDVI anomalies. All anomalies are done with respect to the corresponding mean annual cycle.

Betts–Miller–Janjić (BMJ) convection scheme out-performed the other choices in the region. As in other convective schemes, the decision to activate or not activate deep convection in BMJ is not based entirely upon cloud layer moisture. The reference profiles for the BMJ scheme are calculated by lifting parcels from the boundary layer, so their time dependence responds directly to the land surface forcing and the time dependent response of the mixed layer. For these reasons, alterations to conditions within the planetary boundary layer have an effect on the simulations (K. Betts and Z. Janjić 2013, personal communication). The use of the BMJ scheme is not uncommon in studies of land surface–atmosphere interactions (see, e.g., Xue et al. 2001; Zeng et al. 2012).
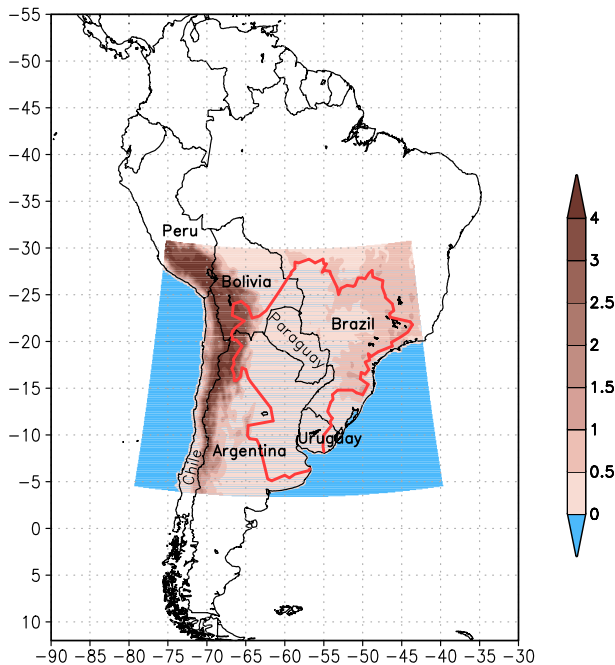
FIG. 3. Model domain and topography. The red line represents the boundary of the La Plata basin.

The model was forced by the initial and 6-h lateral boundary conditions from the NCEP–National Center for Atmospheric Research (NCAR) Global Reanalysis 1 project (Kalnay et al. 1996). Sea surface temperatures were obtained from the Reynolds dataset, also included in the global reanalysis. Soil moisture initial states are an important source of error in the simulations. First, the NCEP–NCAR reanalysis model has a land surface model that is different from the one used in WRF–Noah. Soil moisture estimates are model dependent, and thus the range of values between wilting point and the field capacity can be very different. Second, the reanalysis land surface model has two layers while Noah uses four layers; hence, an interpolation is needed (the interpolation scheme is part of the WRF package). In long-term simulations like the ones performed in this study, the spinup time should be enough to achieve an equilibrium that minimizes these errors.

b. Model evaluation

Control simulations (CTL) were carried out using the USGS land-cover map and its corresponding biophysical properties. Experiments using the International Geosphere–Biosphere Programme (IGBP) land-cover categories obtained from MODIS data were also carried out, but they are not shown as the model performance was similar to that using the USGS definitions. An ensemble of five members was created using identical

parameterizations with the only difference being the initial conditions that are 24-h apart following the lagged average forecasting method (Hoffman and Kalnay 1983). The period of simulation extends from 29 August–2 September 2007 (5 successive initial days) to 31 July 2009 to cover the whole period of precipitation deficit, as shown in Figs. 2a,b. We will call this period the drought period.

The performance of the model was evaluated in terms of precipitation and air temperature at 2 m. The simulation of precipitation is fundamental in the water balance and for the representation of drought events. Models must correctly represent a number of processes (e.g., evapotranspiration, condensation, moisture flux convergence) to simulate the patterns of precipitation. The spatial distribution of the CTL ensemble precipitation (Fig. 4b) follows the satellite-derived precipitation pattern (Fig. 4a), with high values toward the northeast of the domain decreasing toward the southwest. The control ensemble represents the observed precipitation center over northern Bolivia but extends over a larger area extending toward the south over or near the Andes cordillera. Despite the similar precipitation patterns, quantitative differences are found (Fig. 4c). In the southeastern part of the domain, where the drought took place, the model has a dry bias of about 1–2 mm day^{-1}, that is, exaggerating the drought severity. Finally, the model simulations exhibit a wet bias toward the northern part of the drought region (northeast Argentina/east Paraguay), thus failing to represent the local drought features. Positive biases are found in an approximate longitudinal band along 25°–18°S, with values of up to 8 mm day^{-1} near the Andes cordillera and the Brazilian highlands and up to 5 mm day^{-1} in Paraguay. The model 2-m temperature was assessed against the gridded dataset of observations.

Figure 5 presents the average temperature during the drought as estimated from the CPC observations, the CTL ensemble, and their differences. The pattern is not shown over the Andes cordillera because the combination of sparse observations and steep slopes prevents a reliable assessment of the model's surface temperature simulations. Away from the Andes, the model simulations capture the main features of the observed temperature in terms of magnitude and distribution. The simulations also reproduce the observed temperature gradient with maximum values over the central-northern domain decreasing toward the south. The bias pattern shows somewhat warmer temperatures over the middle of the continent and cooler temperatures on a band along eastern coast. Away from the mountains, anomalies range between 0.5° and 2°C in magnitude.
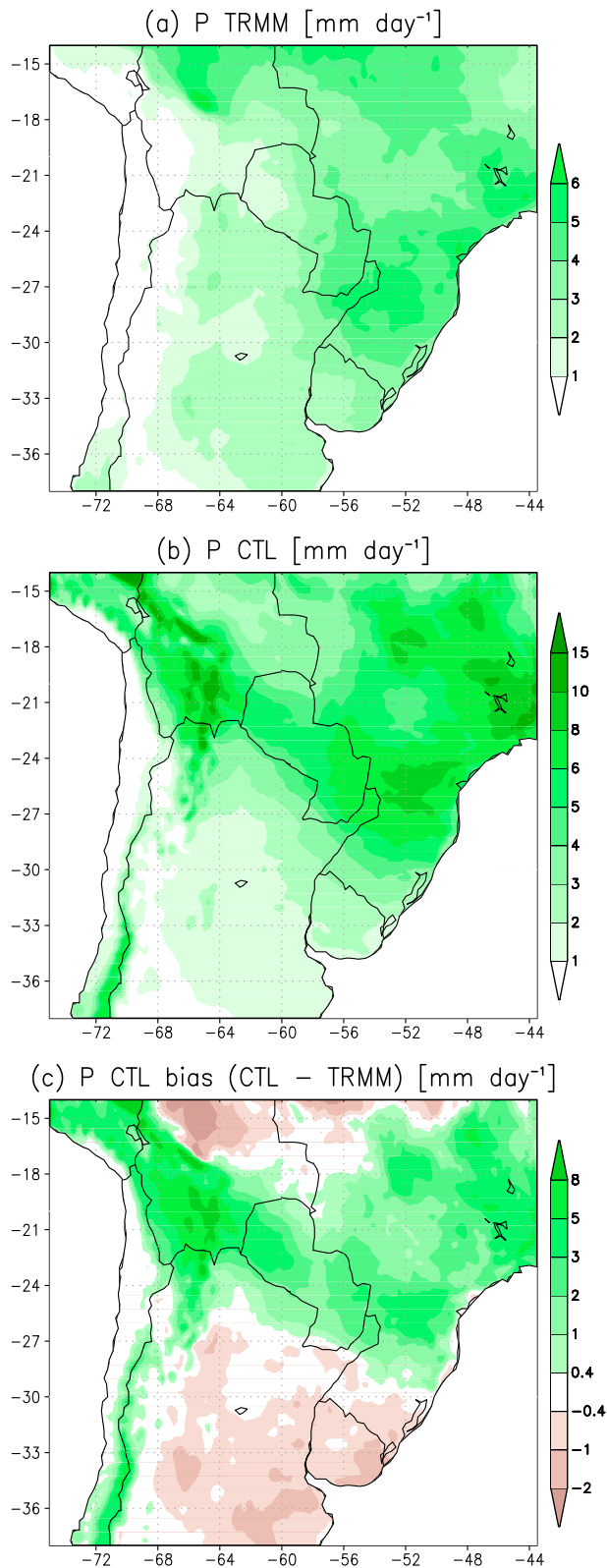
FIG. 4. Mean precipitation during the drought period estimated from (a) TRMM and (b) CTL ensemble and (c) CTL ensemble precipitation biases. Ocean areas were masked out.
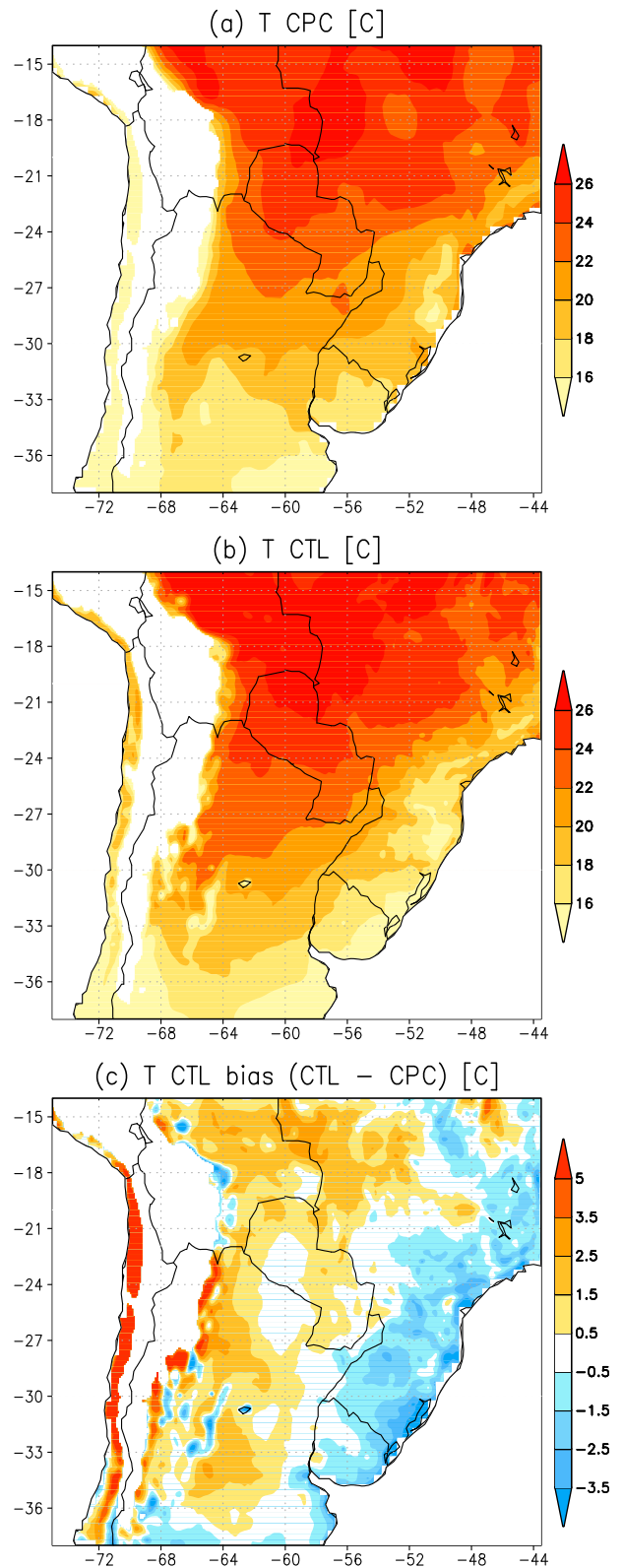
FIG. 5. Mean temperature at 2 m during the drought period estimated from (a) observations and (b) CTL ensemble and (c) CTL ensemble temperature biases. Areas above 800 hPa and ocean areas were masked out.

4. Land-cover properties

The exchanges of energy, water, and momentum between the land surface and the atmosphere depend on the land surface biophysical properties. Consequently, changes in land cover will also affect those exchanges with expected impacts on the climate conditions. This is particularly relevant for southern South America, where the replacement of native vegetation (e.g., by croplands) has extensively occurred in recent years (Volante et al. 2012).

The USGS classification used in the Noah LSM prescribes 24 constant land-cover categories, and each is assigned 15 biophysical properties like rooting depth, minimum and maximum albedo, and surface roughness (Chen and Dudhia 2001). This approach has several limitations since the properties assigned to a given land-cover category are invariant in space and time or are bound by fixed minimum and maximum values: that is, each land cover is assumed to have the same constant properties during a drought or a wet spell and at any location.

a. Ecosystem functional types

To overcome the shortcomings noted above, Lee et al. (2013a,b) explored the sensitivity of climate variables to the use of time-varying ecosystem properties as a replacement of the invariant land-cover types, with promising results for 3-month WRF simulations. Functional attributes of ecosystems, those characterizing the energy and matter exchange between the biota and the atmosphere (Valentini et al. 1999), show a quicker response to environmental changes than structural ones (McNaughton et al. 1989) and are relatively easy to monitor using satellite-derived spectral indices (Paruelo et al. 2001). Based on these concepts, Alcaraz-Segura et al. (2006, 2013b) developed a method to define ecosystem functional types on a yearly basis. Formally, ecosystem functional types are defined as groups of ecosystems that share functional characteristics in relation to the amount and timing of the exchanges of matter and energy between the biota and the physical environment (Paruelo et al. 2001; Alcaraz-Segura et al. 2006). Since EFTs are defined from descriptors of the NDVI dynamics on an annual basis, the year-to-year variability of the surface conditions can thus be identified (Alcaraz-Segura et al. 2013a). Therefore, intermediate and long-term ecological phenomena and land surface processes are better represented: that is, EFTs reflect vegetation changes resulting from either land-use or natural changes.

EFTs are computed using three metrics of the NDVI seasonal dynamics: (i) the annual mean of NDVI as an estimator of net primary production; (ii) the seasonal coefficient of variation of NDVI as a descriptor of seasonality (the difference between the growing and nongrowing season or amplitude of the annual cycle); and (iii) the date of the absolute maximum normalized difference vegetation index in the given year as a phenological indicator of the growing season. For practical reasons (see Alcaraz-Segura et al. 2006, 2013b) the range of values of each NDVI descriptor was divided into four fixed intervals, giving a potential number of $4^3 = 64$ categories. To divide the range of values of the NDVI annual mean into four categories, its three quartiles were obtained for each year and then, for each quartile, the median across years was calculated. The same applies to the seasonal coefficient of variation. Finally, the four categories for the date of maximum NDVI correspond to the four seasons of the year in temperate ecosystems.

The EFTs categories are identified with codes of three characters, one for each descriptor, following the convention suggested by Paruelo et al. (2001). The definition and coding of EFTs allow for an ecological interpretation of the legend in terms of the three NDVI metrics: The first character identifies the net primary productivity from low to high with an uppercase letter from A to D (increasing productivity). The second character represents high to low seasonality (amplitude of the annual cycle), identified by a lowercase letter from a to d (decreasing seasonality). The last character corresponds to the season of the maximum NDVI, where spring is associated with 1 and sequential numbers are for the following seasons. For instance, subtropical rain forests have high productivity, low seasonality, and spring maxima, which correspond to an EFT identified as Dd1. Soybean plantations in the dry Chaco forest have relatively low productivity, very high seasonality, and summer maxima, which correspond to an EFT identified as Ba2. Dry Puna and Patagonia Desert, on the other hand, have very low productivity, very low seasonality, and autumn maxima, which correspond to an EFT defined as Ad3. Humid Pampas have relatively high productivity, very low to low seasonality, and summer maxima, which correspond to EFT categories Ca2 and Cb2.

Figure 6a presents the 2001–09 median EFT field that is a characterization of ecosystem functioning. Warm colors represent ecosystems with large net primary production, low seasonality, and warm season maxima (e.g., the subtropical forests, Dd1). Cold colors represent the opposite behavior, as in the dry Puna (Ad3). See the legend in Fig. 6a for the definition of all ecosystem functional types/colors. Figure 6b shows the 2008 EFTs map. In most of the domain, both maps
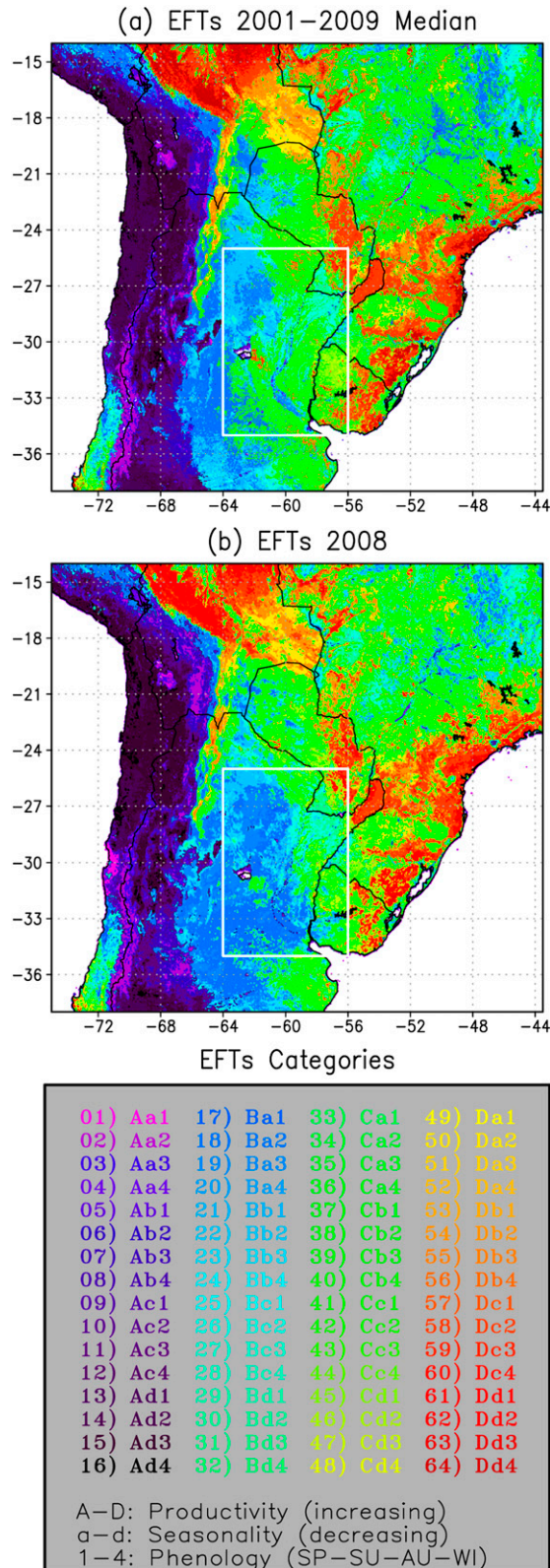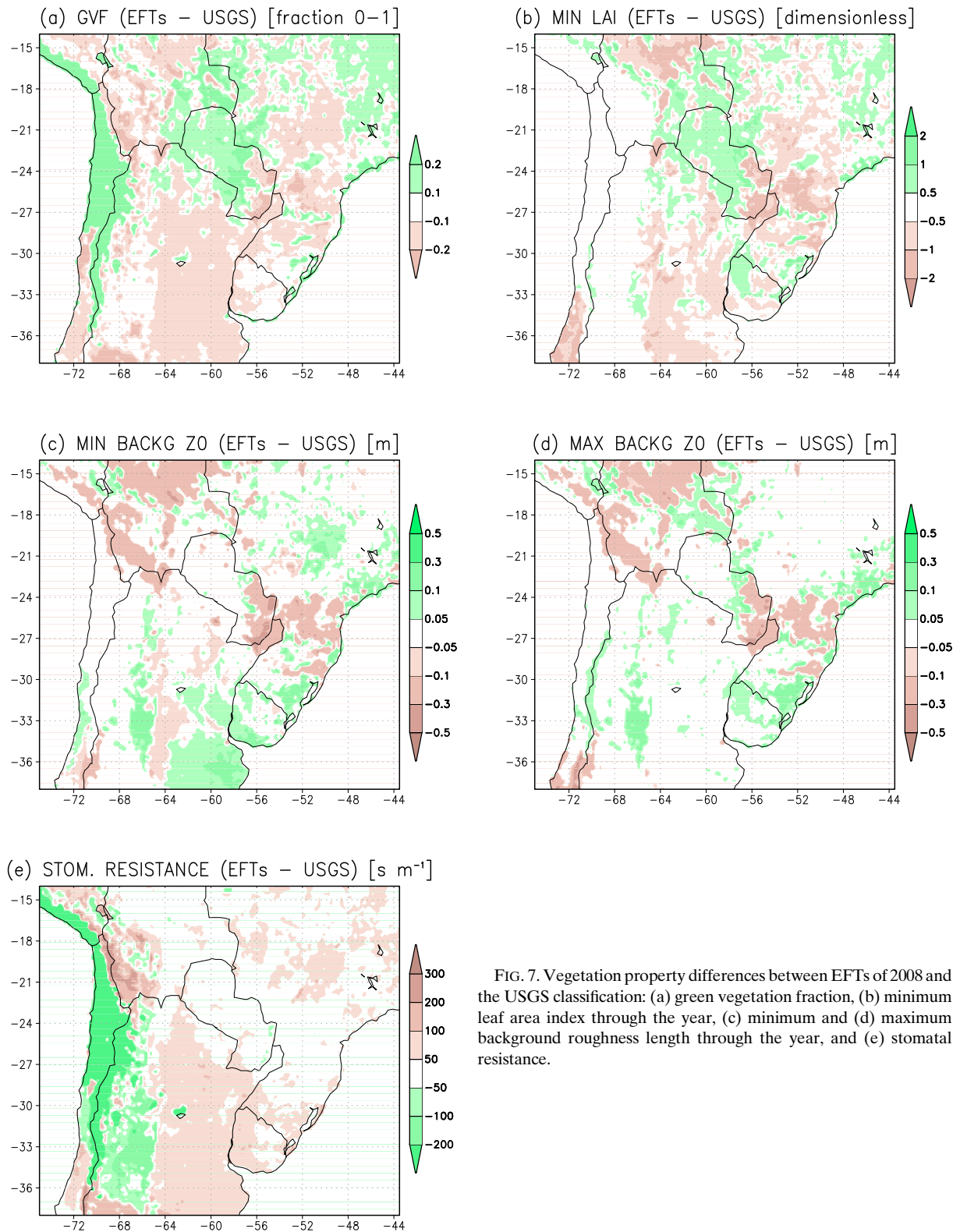
FIG. 6. (a) 2001–09 EFTs median map and (b) EFTs map for 2008. EFTs categories are indicated by the legend at bottom.

(Figs. 6a,b) have similar categories. However, remarkable differences are evident for areas that experienced either strong land-use changes or climate-related vegetation stress. Particularly, the map of 2008 EFTs shows large changes in the main drought area (white rectangle): EFTs that have average productivity (green and light blue categories) in Fig. 6a are replaced by EFTs with low and very low productivity (light and dark blue) during 2008, indicating a reduction in photosynthetic activity. Such interannual changes agree with the observed dynamics in NDVI depicted in Fig. 2e.
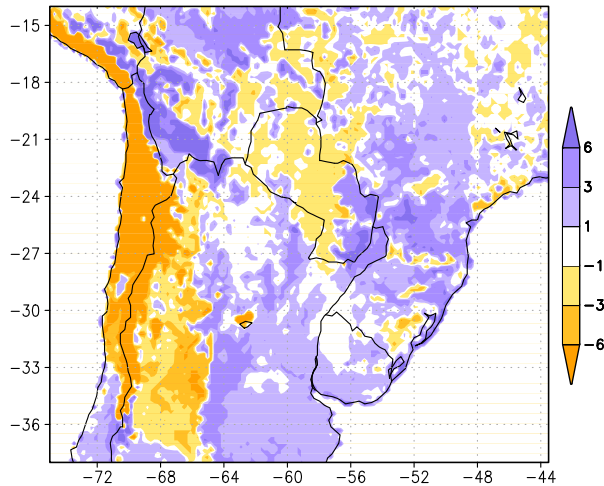
b. A consistent set of time-varying EFT biophysical properties

The Noah LSM defines a table of 15 biophysical properties of each land-cover category of the USGS classification. It also includes a table for use with the IGBP classification. Following the method described in the appendix, an analogous table of properties is obtained for the EFTs categories. The method was applied using the properties of Noah LSM for the IGBP classification over the MODIS land-cover classes (MCD12C1 product, collection 5) (Friedl et al. 2002, 2010). Further details and discussion are provided in the appendix.
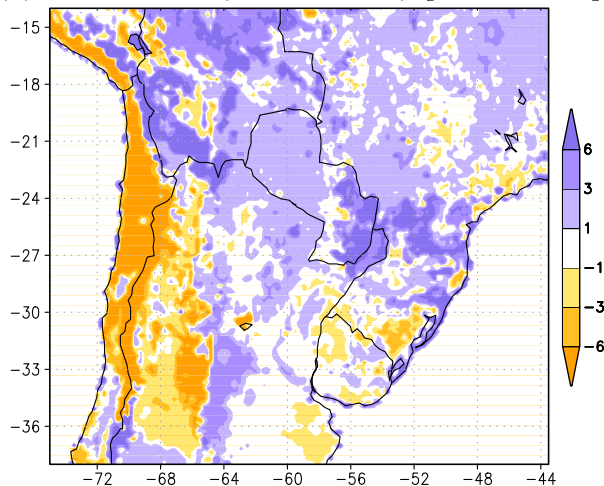
Figures 7 and 8 present the biophysical property changes when the USGS land-cover map is replaced by the EFTs map of 2008. Eight out of the 15 parameters are shown because of their larger dependence on the land surface changes as described by the time-varying EFTs (Alcaraz-Segura et al. 2011, 2013b). Figure 7 presents the properties related to vegetation, like greenness fraction, leaf area index, surface roughness, and stomatal resistance, while Fig. 8 shows properties related to the radiation terms, like albedo and emissivity. Biophysical properties associated with the 2008 EFTs depict the drought region with decreased greenness and leaf area index, and larger stomatal resistance (Fig. 7) as well as an increase in minimum albedo and a reduction of emissivity (Fig. 8). (Note in Fig. 7e that, unlike the rest of the panels, colors were reversed to reflect that, for all properties, green colors represent greener vegetation and brown colors represent drier conditions.) Focusing on the secondary core of the drought (near the tripartite border), EFTs reduce greenness fraction, leaf area index, and surface roughness. This region has higher values of minimum and maximum albedo. While the use of EFTs improves the description of land-cover states in most of the domain, there are exceptions. The Atacama Desert in northern Chile appears greener because the methodology tends to smooth such extreme states.

FIG. 7. Vegetation property differences between EFTs of 2008 and the USGS classification: (a) green vegetation fraction, (b) minimum leaf area index through the year, (c) minimum and (d) maximum background roughness length through the year, and (e) stomatal resistance.

(a) MIN ALBEDO (EFTs – USGS) [frac. 0–100]

(b) MAX ALBEDO (EFTs – USGS) [frac. 0–100]
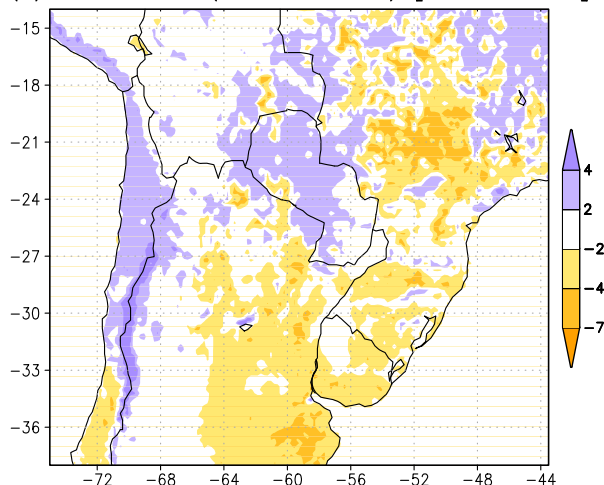
(c) MAX EMISS (EFTs – USGS) [frac. 0–100]

FIG. 8. Vegetation property differences between EFTs of 2008 and the USGS classification: (a) minimum and (b) maximum background albedo through the year and (c) maximum background emissivity through the year.

c. Discussion of the different approaches

As noted earlier, one of the limitations of the conventional USGS or IGBP land-cover types is that they are constant in time. The use of MODIS land-cover categories updated on a yearly basis is an improvement in this respect. Yet, Friedl et al. (2010) report that the MODIS land-cover dataset has an overall accuracy of about 75% but "the range in class specific accuracies is large." The errors may be larger in regions with scarce or no in situ information (e.g., southern South America) than over other regions like the United States or Europe where observations can be used to better define parameters. MODIS also estimates some biophysical properties like green vegetation fraction, leaf area index, and albedo that have begun to be introduced in land surface and climate modeling to depict more realistically some land surface processes (Miller et al. 2006; Weiss et al. 2012). However, there are other parameters like rooting depth or surface roughness length (Z0) that should change consistently with the modified properties but for which there are no satellite estimates. Additionally, the MODIS leaf area index is derived from other MODIS products including the MODIS land cover, which, as noted by Friedl et al. (2010), may be subject to uncertainties. In this work, greenness vegetation fraction, leaf area index, and albedo are derived from EFT values along with all the other biophysical parameters to maintain the consistency among them and avoid mixing approaches. In this way, the dataset has changes in all properties corresponding to a unique physical indicator (the EFT values). In any event, the purpose of this study is not to compare against MODIS estimates but rather to show possible improvements over a current version of the WRF–Noah that is of common use.

Note that with the conventional approach it is also possible to increase the number of land-cover types to better represent shifts in crop types (see Beltrán-Przekurat et al. 2012), something that has occurred intensively in the region of interest (changes within the cropland category have involved soy bean, alfalfa, and wheat, among other crop types). Nevertheless, assigning physical properties to each subcategory may be hard to achieve. In our case, the EFT properties are derived from the smaller number of land-cover types, which is done as weighted averages for each pixel. Per se, this may not provide additional information; however, EFTs include in their definition a representation of vegetation status by means of the primary production, annual amplitude, and phenology of the NDVI annual cycle at pixel level, ecologically meaningful information that otherwise would not be taken into account.

The definition of EFTs captures the differences in ecosystem functioning within the same land-cover type. For instance, it distinguishes dense from open shrub lands or irrigated from rain-fed croplands by means of their differences in primary production dynamics. With these definitions, yearly changes in EFTs (either land-cover changes or interannual variability of environmental factors) will have associated a consistent set of yearly biophysical properties (e.g., a dry year with stressed vegetation will have increased stomatal resistance, higher albedo, and lower surface roughness and the opposite during a wet year).

Summarizing the key aspects of the EFTs classification, it is noted that (i) it is an alternative approach to land-cover classification that centers on physical properties that allow one to identify patches of land that behave homogeneously in terms of surface–atmosphere energy and biomass exchanges (for a same EFT value) (from a climate modeling point of view, this is unique); (ii) it is based in concepts of ecosystems functions, energy and carbon exchanges; (iii) it can be applied to cases preceding the MODIS period (using AVHRR NDVI); and (iv) it provides consistency among changes in all 15 biophysical parameters.

5. Effects of land surface changes on regional climate

The sensitivity of the model to the lower boundary conditions was tested for the period that included the 2008 severe drought. Long-term simulations with the WRF–Noah model were performed using the land-cover representation based on EFTs properties described in section 4, and the results were compared with the control simulations. The model configuration for the EFT ensemble simulations was identical to that of the CTL ensemble, except for the change in the land-cover dataset. An analysis is done of the changes in precipitation and 2-m temperature changes when EFTs are used as lower boundary conditions. The interpretation of these changes focuses on the modification of vegetation properties and concurrent land surface processes. Nevertheless, a specific interpretation for the precipitation and 2-m temperature changes is not always apparent owing to the complexity of the system, including the type of land cover (or EFT) that prevails in each region and the dominant precipitation/circulation regimes to which each region is subject. Further, while the Noah LSM follows a single column approach, its use over a grid and coupled with WRF implies that nonlinear three-dimensional effects will take place. Land-cover changes will favor the generation of surface gradients for different variables, which in turn will
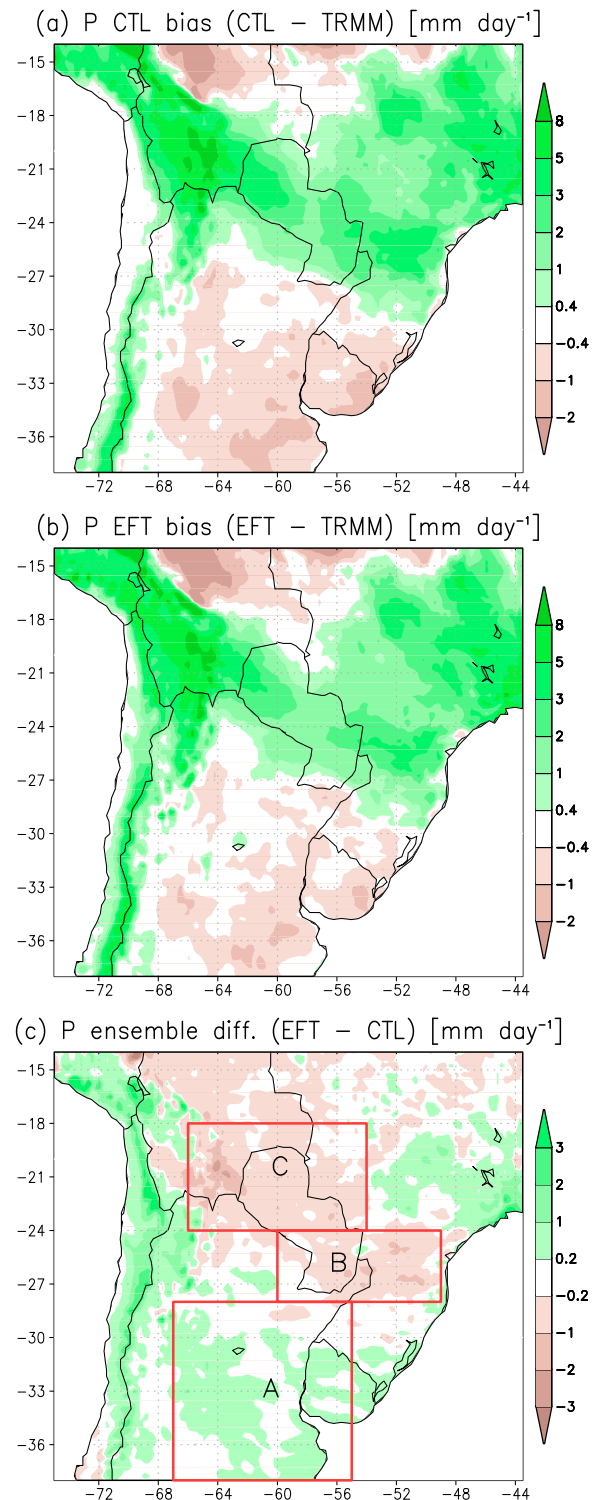

FIG. 9. Mean precipitation during the drought period: (a) CTL ensemble, (b) EFT ensemble, and (c) their differences. In (c), the three regions identified are selected for further analysis: A represents the drought region, B represents the northernmost part of the drought area, and C is the region with large positive biases of precipitation. Ocean areas were masked out.
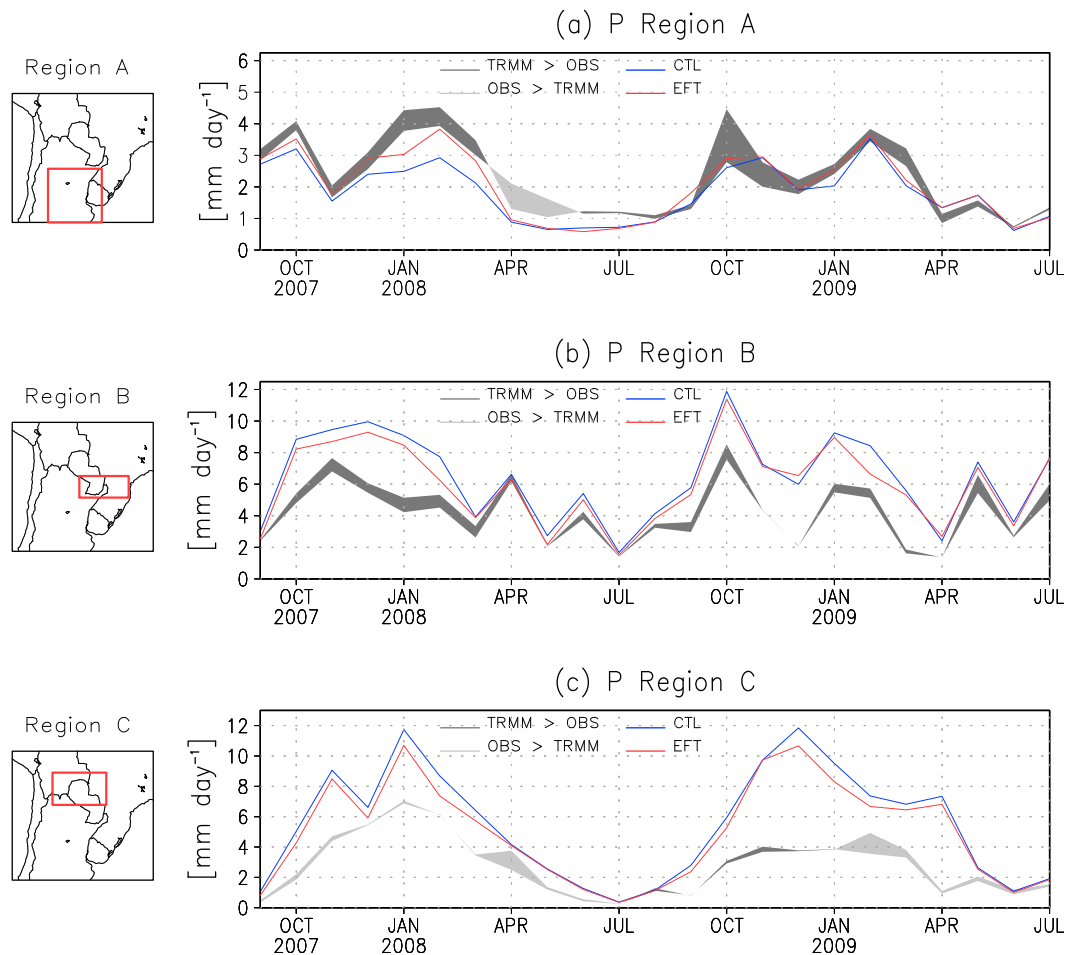
FIG. 10. Land-only area-averaged precipitation for TRMM and observations (OBS) (their differences are shaded) CTL and EFT ensembles over (a) region A, (b) region B, and (c) region C.

induce local circulations and differential surface heat fluxes. Advective processes will be influenced, as will be the moisture flux convergence (e.g., Baidya Roy and Avissar 2002; Lee and Berbery 2012).

a. Land surface effects on precipitation

Figure 9 compares the model rainfall biases for the CTL and EFT ensembles during the drought period. As discussed in section 3b, the CTL simulations underestimate rain in the main drought area (Fig. 9a) and overestimate precipitation in the northern part of the domain, over the Andes cordillera, the Brazilian highlands, and Paraguay. The rainfall bias of the EFT ensemble (Fig. 9b) resembles that of the CTL ensemble in terms of both pattern and magnitude. Nevertheless, the difference map (Fig. 9c) shows that the EFT ensemble reduces the biases in several regions. To the south of the domain, positive values (green shades) mean that the EFT ensemble produced slightly more rain in an area

where the CTL had a dry bias. Over Bolivia, Paraguay, and southern Brazil, Fig. 9c presents negative values (brown shades), meaning that the EFT ensemble reduces the wet bias of the CTL ensemble. Thus, the EFTs bring the model representation of the precipitation pattern closer to the observations in regions with either wet or dry biases.

Three regions were selected to examine the time evolution of area-averaged model, satellite, and observed precipitation estimates (Fig. 10). The shading between the satellite and observed precipitation is an indicator of the uncertainty in the observations, and mean biases are presented in Table 1. Region A covers the drought core where the CTL ensemble simulations exaggerate its severity (Fig. 4c). The EFT ensemble simulation increases the magnitude of the precipitation (Fig. 10a), reducing the dry bias by about 8.5% during the summer (Table 1) and offering a somewhat better representation of the drought event. Region B corresponds to

TABLE 1. Bias reduction in precipitation from the CTL ensemble to the EFT ensemble for the three regions defined in Fig. 9c.

Region	Drought period	Summer (Dec–Feb)
A	3.90%	8.46%
B	7.98%	11.29%
C	18.30%	21.62%

the northern sector of the observed drought, where the model had failed to replicate the dry conditions. The EFT ensemble precipitation (Fig. 10b) remains at all times closer to the observations than the CTL ensemble, indicating again an improvement on the simulation. Here, the wet bias was reduced by 8% for the whole period and by 11.3% during summer. Notably, despite differences in magnitude and the absence of a well-established annual cycle, the model simulations reproduce the month-to-month variability. Finally, region C covers northern Paraguay/southern Bolivia where the CTL ensemble exhibits a large wet bias. The observed rainfall (Fig. 10c) has a defined annual cycle with a maximum during austral summer and a minimum during winter. The evolution is correctly represented in the two ensemble simulations, but with excessive magnitude during summer, sometimes more than doubling the observed values (e.g., December 2008). However, the EFT ensemble simulation reduces the wet bias by 18.3% for the whole period and 21.6% for the rainy season (Table 1).

The EFT ensemble vegetation for region A seems to be more representative of the drought period than the CTL ensemble, as it exhibits a lower vegetation greenness fraction and leaf area index, as well as higher stomatal resistance (Table 2). On the other hand, the EFT ensemble has a precipitation increase over region

A that cancels out the dry bias noted in the CTL ensemble. The increased precipitation leads to soil moisture increases, favoring a larger latent heat flux and a sensible heat flux reduction (Fig. 11). While the two findings (bias reduction and more realistic vegetation representation) are encouraging when considered independently, together they seem counterintuitive. A plausible justification can be found in Lee and Berbery (2012) who examined the effects of land-cover changes in the La Plata basin, where region A is located. Their results indicate that land-cover changes also induce changes in lower-level moisture fluxes and their convergence. In the case of the current study, land-cover changes from the CTL to the EFT ensembles induce an increase of about 25% of the vertically integrated moisture flux convergence (not shown) that helps explain the increase of precipitation as a larger-scale effect of land-cover changes as opposed to a local effect alone.

The reduction of precipitation (P) to the north of the domain (brown shades over regions B and C in Fig. 9c) is associated in general terms with a reduction of all components of the surface water balance: soil moisture (SM), evapotranspiration (EVT), runoff, and precipitation (see Table 3). Table 2 shows 10 out of the 15 biophysical properties for the three regions. The five terms excluded either did not give perceptible information for the region (e.g., related to snow processes or radiation stress) or were mostly constant (e.g., rooting depth). According to Table 2, the EFTs properties in region B are more representative of drier conditions than those obtained from USGS, with a reduction of the green vegetation fraction and the leaf area index and increasing stomatal resistance. The large negative difference in surface roughness is likely attributable to the replacement of subtropical humid forests by crops in

TABLE 2. Area-averaged values of vegetation properties for the three selected regions (A, B, and C) derived from the USGS land-cover dataset and the EFT datasets. Their percent differences are computed as [(EFTs − USGS)/USGS] × 100. The properties are green vegetation fraction (fraction 0.0–1.0), stomatal resistance (s m^{-1}), minimum and maximum leaf area index through the year (dimensionless), minimum and maximum roughness length through the year (m), minimum and maximum albedo through the year (fraction 0.0–1.0), and minimum and maximum emissivity through the year (fraction 0.0–1.0).

|	A			B			C		
	USGS	EFTs	Diff (%)	USGS	EFTs	Diff (%)	USGS	EFTs	Diff (%)
GVF	0.73	0.64	−12.3	0.77	0.73	−5.2	0.62	0.68	9.7
Stomatal resistance	94.57	128.01	35.4	103.21	115.94	12.3	90.66	122.87	35.5
LAI min	1.24	0.97	−21.8	1.98	1.53	−22.7	1.00	1.20	20.0
LAI max	4.03	3.50	−13.2	4.97	4.42	−11.1	3.99	3.99	0.0
Z0 min	0.09	0.12	33.3	0.31	0.21	−32.3	0.19	0.16	−15.8
Z0 max	0.14	0.16	14.3	0.31	0.24	−22.6	0.19	0.19	0.0
Albedo min	0.18	0.19	5.6	0.16	0.18	12.5	0.19	0.19	0.0
Albedo max	0.22	0.22	0.0	0.17	0.20	17.6	0.20	0.22	10.0
Emissivity min	0.93	0.93	0.0	0.94	0.93	−1.1	0.93	0.93	0.0
Emissivity max	0.97	0.95	−2.1	0.95	0.95	0.0	0.94	0.95	1.1
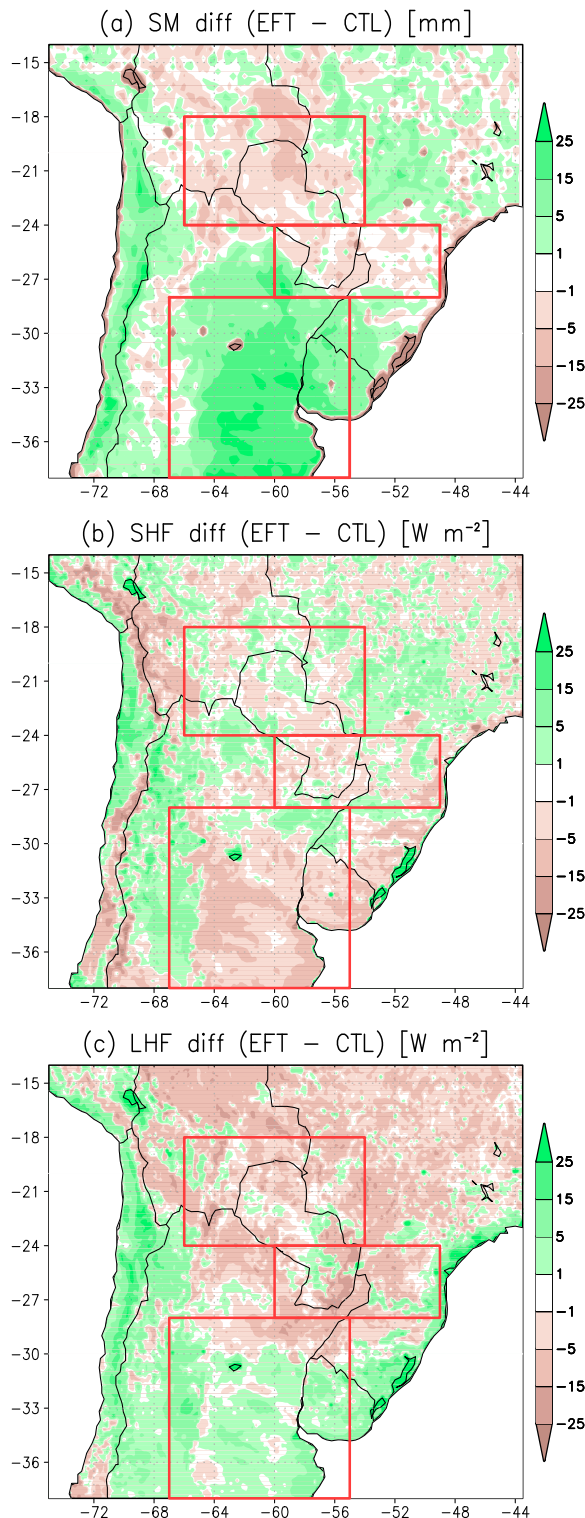
FIG. 11. Mean values during the drought period of (a) soil moisture for the top two layers (40-cm depth), (b) sensible heat flux (SHF), and (c) latent heat flux (LHF). (The positive soil moisture differences over region A correspond to the reduction of the dry bias. See text for details.)

recent decades (Izquierdo et al. 2008). These conditions increase the surface resistance to evaporation, giving place to a positive feedback with weaker turbulent exchanges, lower precipitation, soil wetness, and runoff (Fig. 11 and Table 3). Note that the mean values of soil moisture in the CTL and EFT ensembles are similar (Table 3). Analysis of the spatial patterns (Fig. 11a) indicates that this is attributable to the large positive differences of soil moisture around the southwestern sector of region B. However, over most of the area where the precipitation bias reduction was achieved, the use of EFTs leads to a general reduction of soil moisture.

The reduction of evapotranspiration in region C (Table 3 and Fig. 11c) can be traced to the increased stomatal resistance and the smaller roughness length (Table 2), consistent with a reduction of the turbulence in the boundary layer and an increase of the lower atmosphere stability. Also, the decrease in the total heat flux (Figs. 11b,c) reduces the moist static energy at the boundary layer (Eltahir 1998) and favors lower rainfall, as shown in Fig. 9c. As a result of these changes, precipitation, soil moisture, and runoff are also reduced (Table 3).

In summary, the results show that areas where soil moisture is reduced are associated with evapotranspiration reductions, sensible heat flux increases, and lower precipitation and runoff. Conversely, regions where the soil moisture has increased are associated with sensible heat flux reductions and latent heat flux increases that favor a moister boundary layer and increased rainfall and runoff. Correlations among soil moisture, heat fluxes, and precipitation presented in Table 4 support these general conclusions. Soil moisture is positively (negatively) correlated with latent heat flux (sensible heat flux). In turn, the correlation between latent heat (sensible heat) and precipitation is also positive (negative). These results agree in general terms with the theory of Eltahir (1998) who proposes a pathway for relating the positive feedback between soil moisture conditions and rainfall. As discussed, deviations from this behavior are found when regional circulations develop also as a result of land-cover changes.

b. Land surface effects on 2-m temperature

The 2-m temperature bias of the CTL ensemble simulation was discussed in section 3b and depicts a large-scale pattern of negative values (cold bias) toward the east coast over Uruguay and southern Brazil and positive values (warm bias) over the central continental region east of the Andes (Fig. 12a). Figure 12b presents the differences between the CTL and EFT biases, showing a general increase of 2-m temperature. To further the analysis of the biases, two key regions,

TABLE 3. Area averages (regions A–C) of selected variables from the CTL and EFT ensembles and their differences computed as $[(EFT - CTL)/CTL] \times 100$. The variables are precipitation (mm day^{-1}), soil moisture (mm), evapotranspiration (mm day^{-1}), and runoff (mm day^{-1}). Only data over land were considered.

	A			B			C		
	CTL	EFT	Diff (%)	CTL	EFT	Diff (%)	CTL	EFT	Diff (%)
P	1.85	2.05	10.8	6.44	6.03	−6.4	5.45	4.97	−8.8
SM	86.44	97.74	13.1	136.79	136.90	0.1	113.58	111.83	−1.5
EVT	1.58	1.66	5.1	3.32	3.18	−4.2	2.88	2.73	−5.2
Runoff	0.19	0.24	26.3	2.76	2.48	−10.1	2.14	1.82	−15.0

identified as central and eastern in Fig. 13, were examined. Table 5 presents the values of the biophysical properties for USGS and EFTs and their differences, while Table 6 shows the values of surface variables related to the energy balance from the corresponding ensembles (CTL and EFT). According to Fig. 13a, the cold biases in the CTL simulation are present during all months but with somewhat larger values during the warm season. The EFT simulation exhibits a larger amplitude of the temperature annual cycle and, while maintaining a negative bias during the cold season, it eliminates the negative bias in summer (in fact, it overcorrects, showing a slightly positive bias). Overall, the cold bias in the CTL ensemble in the eastern sector averages −1.3°C, but it is notably reduced in the EFT ensemble to 0.2°C with a reversal of its sign (Fig. 13a). Contrary to what might be expected in the central region (Fig. 13b) the overall EFT ensemble 2-m temperature bias is larger than the CTL ensemble bias (1.4° versus 0.5°C). The EFT simulation reduces the positive bias during the winter months, but increases them during the warm season.

The general warming over much of the domain can be attributed to the reduction of vegetation, as indicated in the changes of green vegetation fraction and leaf area index for the EFT ensemble (see Table 5 and Figs. 7a,b). This argument is consistent with other studies investigating the relations between vegetation and surface temperature (see, e.g., Kaufmann et al. 2003; Seneviratne et al. 2010; Avila et al. 2012). The changes in vegetation can be attributed to the drought conditions, although the replacement in recent years of natural forest by sowing and crops to the north of the region (Izquierdo et al. 2008), which are not represented in the CTL land cover, may have contributed as well. Despite the consistent result for vegetation changes and temperature changes, the analysis of the energy balance (Table 6) is uncertain. Most of the changes in the energy budget terms are small and do not appear to have physical consistency. Obviously, the 2-m temperature does not match uniquely the energy balance (surface temperature does); however, at this stage and without analysis beyond the

scope of our study, it is unclear whether those inconsistencies are due to differences of behavior between the 2-m temperature and the surface temperature, changes on circulations patterns that introduce large nonlinearities, or simply the surface energy term variations are at a noise level.

6. Discussion: Evolution of the drought

So far the analysis focused on the differences between the CTL and EFT ensembles. Here the drought period will be examined against a mean climatology, where anomalies are computed as the differences between the results of the EFT ensemble and mean values of a 10-yr model climatology (2001–10). (The climatology itself will not be discussed in this article.) Figure 14 presents the evolution of the anomalies of rain, soil moisture, latent and sensible heat flux, and temperature averaged for the main drought area (corresponding to 38°–28°S, 63°–55°W). The evolution of the simulated precipitation anomalies (Fig. 14a) is remarkably similar to the satellite and observed precipitation anomalies shown in Figs. 2a,b, with an almost continuous deficit of rain from November 2007 to June 2009 and the largest drynesses in November 2007, April and December 2008, and March 2009.

The soil moisture anomalies (Fig. 14b) have a delayed response to the precipitation anomalies and show dry conditions beginning in March 2008 and continuing until July 2009, with only February 2009 having a slightly positive anomaly. During June–October 2008, precipitation was closer to normal values, which allowed the soil

TABLE 4. Correlation coefficients between ensemble changes (EFT − CTL) of soil moisture, heat fluxes, and precipitation.

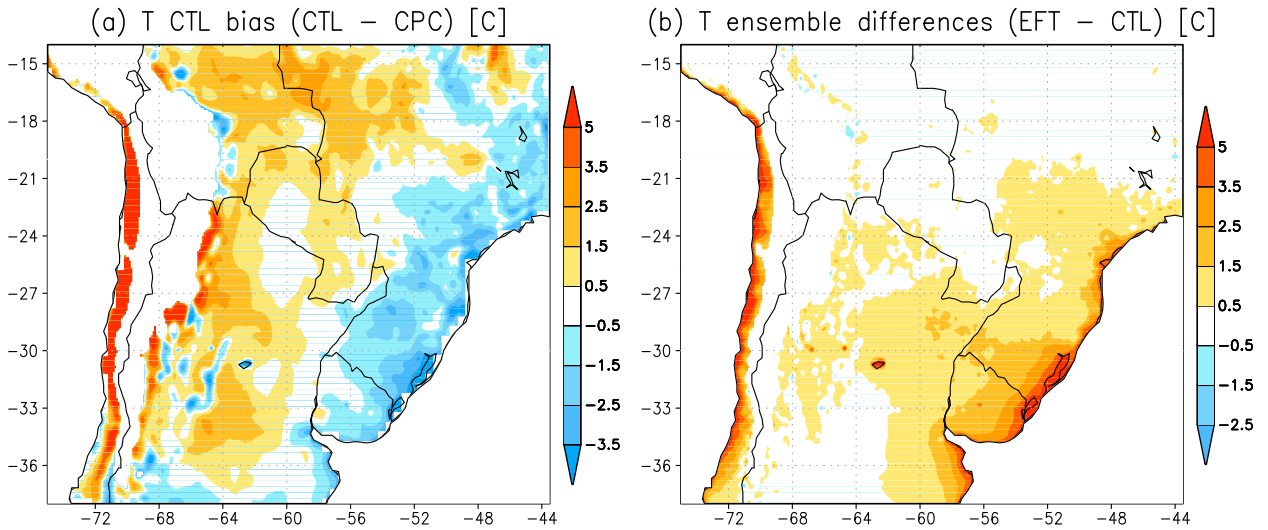|	Region		
	A	B	C
SM − LHF	0.83	0.62	0.84
SM − SHF	−0.67	−0.78	−0.91
LHF − P	0.67	0.06	0.71
SHF − P	−0.24	−0.60	−0.74

FIG. 12. Mean 2-m temperature during the drought period: (a) CTL ensemble bias and (b) differences between the EFT and CTL ensembles. Areas above 800 hPa and ocean areas were masked out.

moisture to recover partially and reduce the anomalies during the austral 2008/09 summer. This feature is not found in the CPC soil moisture estimates (Fig. 2c), although the overall evolution is consistent with them.

The negative anomalies of the latent heat flux for the whole period (Fig. 14c) indicate a continuous deficit of evapotranspiration, which can be associated with the increased vegetation stress owing to the lack of water. The evolution of the sensible heat flux (Fig. 14d) closely follows the climatology with alternating periods of

small negative and positive values. Note the negative relation between sensible and latent heat fluxes, with sensible heat flux being positive at the time of largest negative latent heat flux anomalies. The temperature time series shows that the drought region was about 2°–3°C warmer than normal, except during winter.

In summary, the dry soil conditions and lower normalized difference vegetation index reported in section 4 during the drought modified the spatial distribution of some properties like green vegetation fraction, albedo,
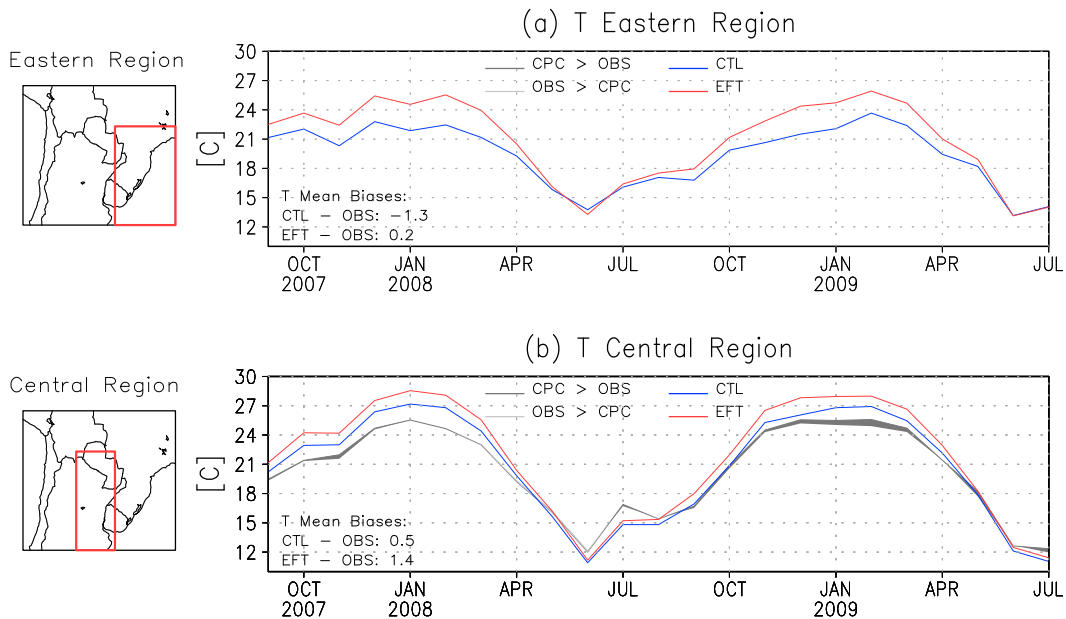

FIG. 13. Area-averaged 2-m temperature for CPC and OBS (their slight differences are shaded) CTL and EFT over two regions denoted to the left: (a) eastern region and (b) central region. Only data over land were considered.

TABLE 5. As in Table 2, but for the eastern and central regions.

	Eastern			Central		
	USGS	EFTs	% diff	USGS	EFTs	% diff
GVF	0.37	0.35	−5.4	0.70	0.67	−4.3
Stomatal resistance	92.95	106.77	14.9	61.99	116.99	88.7
LAI min	0.90	0.74	−17.8	1.17	1.09	−6.8
LAI max	2.18	2.14	−1.8	4.09	3.79	−7.3
Z0 min	0.12	0.10	−16.7	0.13	0.14	7.7
Z0 max	0.12	0.12	0.0	0.16	0.18	12.5
Albedo min	0.12	0.13	8.3	0.18	0.19	5.6
Albedo max	0.13	0.14	7.7	0.21	0.22	4.7
Emissivity min	0.96	0.96	0.0	0.92	0.93	1.1
Emissivity max	0.97	0.96	−1.0	0.96	0.95	−1.0

TABLE 6. Area averages for the central and eastern regions of selected variables from the CTL and EFT ensembles and their differences computed as $[(\text{EFT} - \text{CTL})/\text{CTL}] \times 100$. The variables are temperature (°C), net radiation (W m^{-2}), sensible heat flux (W m^{-2}), and latent heat flux (W m^{-2}). Only data over land were considered.

	Eastern			Central		
	CTL	EFT	% diff	CTL	EFT	% diff
T	19.49	20.85	7.0	20.88	21.74	4.1
NR	128.13	126.46	−1.3	120.58	117.80	−2.3
SHF	37.94	38.76	2.2	55.04	54.03	−1.8
LHF	85.64	86.58	1.1	62.54	61.96	−0.9

surface roughness length, and stomatal resistance. When rain is strongly reduced with respect to the climatological values, temperatures are larger than normal, latent heat flux decreases, and sensible heat flux increases. The soil moisture is also reduced, with a delay due to memory processes. Low evapotranspiration leads to deficient atmospheric moisture, increasing the stability of the lower atmosphere and intensifying the downward trend of rainfall.

7. Conclusions

Recent efforts have produced a number of high-quality remotely sensed land-cover maps that can be used to better represent the land surface states and the land–atmosphere interactions, improving the performance of climate models. Our work contributes to this line of research by presenting a new approach to describe vegetation in regional models with information obtained from satellite-based estimates of ecosystem functional properties. New time-varying maps of the land surface biophysical properties were created using ecosystem functional types, which capture the changes of vegetation status owing to anomalous climate conditions as well as changes due to land-use practices. This approach ensures the use of a consistent set of biophysical vegetation properties that reflect actual land surface conditions in long-term simulations with WRF. The method should be most helpful when actual conditions depart from mean values as it happens during extreme events. To confirm this hypothesis, this study focused on land surface processes during the 2008 severe drought in southern South America while also examining other regions where model biases were large.

Simulations using the standard surface conditions (USGS land-cover map) represent the spatial pattern of precipitation but tend to exaggerate the drought severity while producing large excesses of precipitation in other regions. The temperature is reasonably well simulated in magnitude and distribution, except for cold biases toward the eastern coast and large biases over the Andes cordillera and its eastern slopes. Vegetation changes due to the drought or to land-use changes modify the spatial distribution of the surface biophysical properties. The use of the new dataset of EFT-based vegetation properties as a replacement of the conventional land-cover types in the WRF–Noah model offers evidence that time-varying land-cover properties do impact the performance of coupled land–atmosphere models. Particularly, the use of the novel EFT dataset leads to an improvement of the drought simulation and reduces the wet biases in most (but not all) regions of large precipitation. The results show that the model is sensitive to land-cover changes and vegetation variability through land–atmosphere interactions.

Precipitation estimates showed improvements in most regions, but mixed results were obtained for the temperature bias: The use of EFTs produced a significant reduction of the negative anomalies of temperature (cold bias) toward the eastern part of the domain over land. On the other hand, the near-surface temperature simulation was degraded over the central region where the warm bias was increased by about 1°C. The reasons for this inconsistency are not yet understood and may be inherent to parameterizations that tend to tune terms for better results. While beyond the scope of this work, further examination will require to combine the study of surface states with corresponding changes in parameterizations. Advective processes have not been discussed in this article, but there are indications that they may play an additional role in defining temperature in this region.

The EFTs approach allows a suitable characterization of the actual surface conditions (the state of the vegetation), which is the bottom boundary condition for model simulations (e.g., WRF–Noah, as applied to this study). With near-real-time availability of EFT datasets, the method may have implications for numerical weather
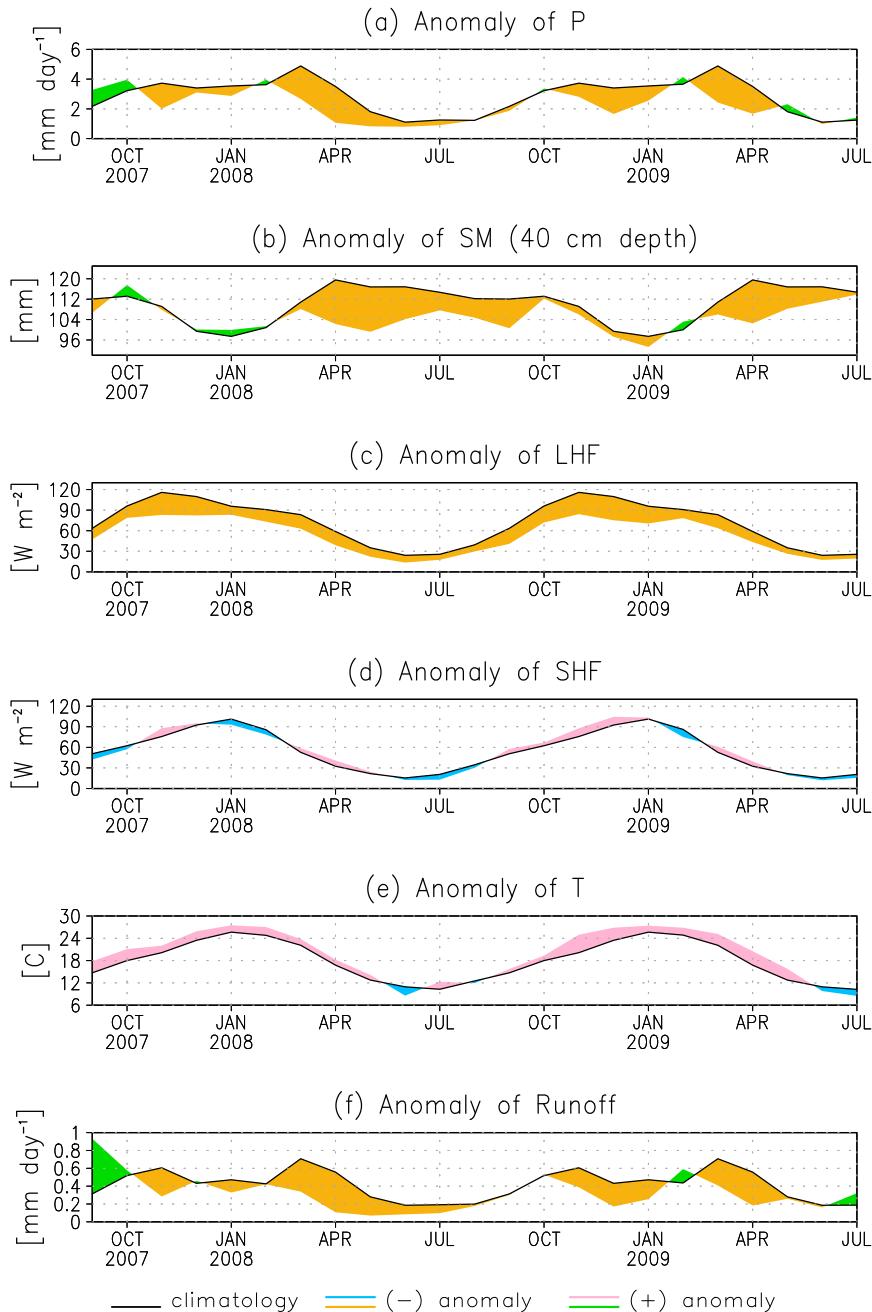
FIG. 14. Land-only area-averaged anomalies for the main drought area of (a) precipitation, (b) soil moisture, (c) latent and (d) sensible heat fluxes, (e) temperature at 2 m, and (f) runoff. The anomalies were computed as the difference between the variables of the EFT ensemble and climatology variables from a 10-yr simulation (2001–10).

prediction as well so that this approach could be used for both weather and climate models.

NCEP operations currently use fixed land-cover types and an older 5-yr climatology of green vegetation fraction (GVF), which is derived from NDVI data. NCEP is exploring the use of a near-real-time GVF product and the use of the future Noah LSM with multiparameterization options (Noah-MP), which has CO_2-based photosynthesis, an explicit canopy, and dynamic (growing) vegetation, among other upgrades (Niu et al. 2011). A desired next step will be to combine the methodology presented here with the future Noah-MP. One additional consideration is that, for operational numerical weather prediction and seasonal climate forecasting, EFTs need to smoothly vary
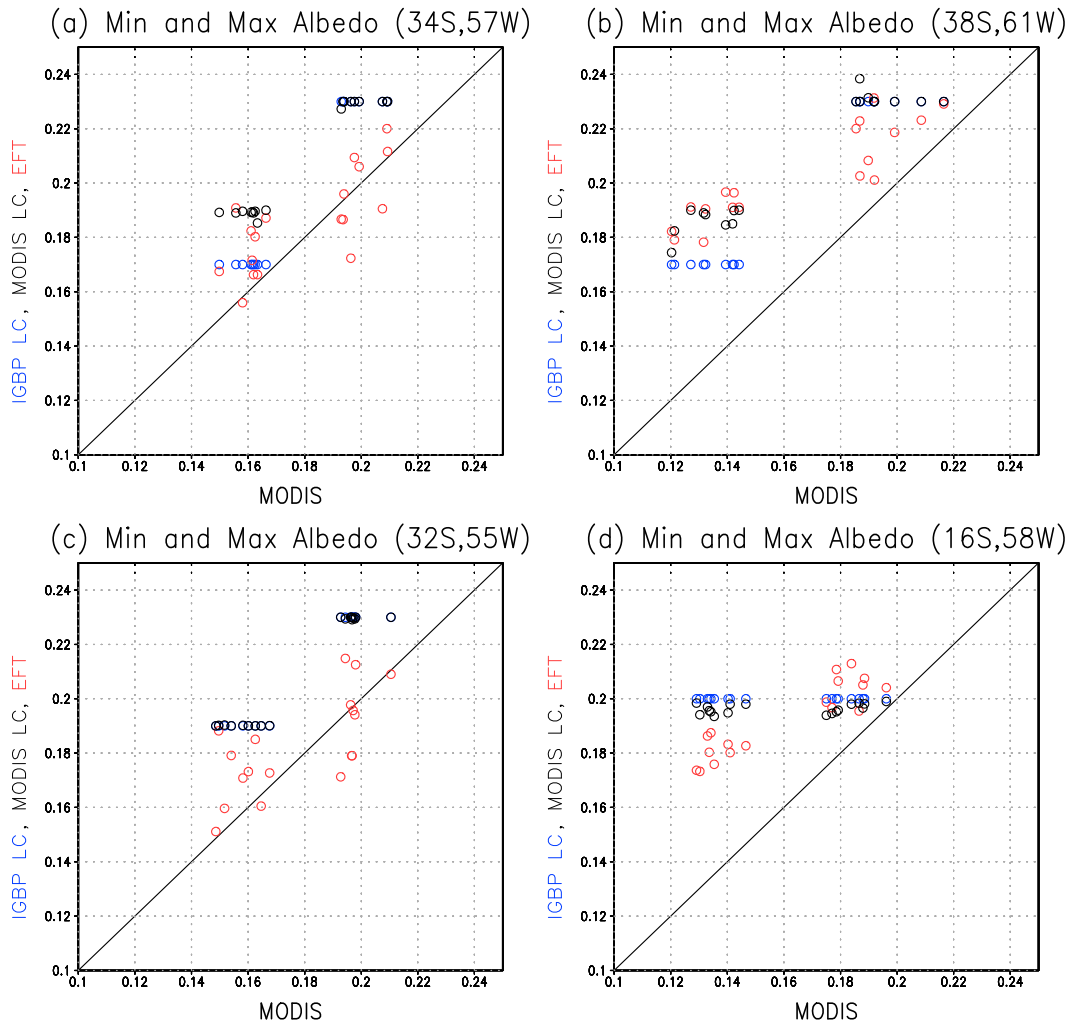
FIG. A1. Scatterplots of MODIS albedo (product MCD43C3) vs albedo derived from IGBP land-cover categories (blue); vs albedo derived from MODIS land-cover product MCD12C1 (black); and vs albedo derived from EFT categories (red). [Blue and black circles overlap in (c).] The corresponding IGBP land-cover categories for the selected points are (a) croplands (34°S, 57°W); (b) croplands (38°S, 61°W); (c) grasslands (32°S, 55°W); and (d) savanna (16°S, 58°W).

from season to season or year to year, similar to the near-real-time GVF derived from weekly observed NDVI that NCEP plans to use. In that case, it will be necessary to explore how the near-real-time GVF maps can be best combined with the 64 EFT categories.

APPENDIX

Computation of the EFT Biophysical Properties

Once the EFT categories are defined (section 4), the computation of their corresponding biophysical properties is done following these steps.

1) Each 0.05° MODIS pixel in the MCD12C1 product comes with the percentage coverage of IGBP land-cover classes for each year.

2) The MODIS land-cover classes were then used to specify 15 land surface parameters (as defined by a table in the Noah LSM: land-cover class → values for 15 parameters) for each pixel and each year. These parameters are fixed for each land-cover class. For each 0.05° MODIS pixel, we calculated a 15-parameter weighted average value (one for each land surface parameter) based on the percentage coverage of each IGBP class.

3) Each MODIS pixel was also assigned a particular EFT category (from 1 to 64) for each year. The 64 annual EFT categories were computed from the monthly NDVI values of the MOD13C12 product (Alcaraz-Segura et al. 2013b).

4) The annual EFT maps were then overlaid on top of each of the 15 land surface parameter maps of the corresponding year (from step 2). Then, for each EFT category, a spatially averaged parameter value was computed. This means that we have now for each year a table with a set of 15 biophysical parameters per EFT category.

5) Finally, the 2001–09 time mean of each land surface parameter was computed for each EFT category. With this step we get a unique relation between EFT categories and their biophysical parameters that allows us to prepare a unique table similar to the one used in Noah LSM (EFT category → values for 15 parameters).

To test the performance of the approach, minimum and maximum albedo scatterplots from different sources were contrasted for four different locations. Following the IGBP classification, the locations are identified as croplands (two areas), grasslands, and savanna. The albedo estimates are as follows: (i) MODIS albedo product MCD43C3, shortwave, used as reference; (ii) IGBP land cover (LC)-derived albedo using the corresponding conversion table provided by the Noah LSM; (iii) MODIS LC-derived albedo computed as for IGBP LC but using the MODIS land-cover types, product MCD12C1; and (iv) EFTs albedo (derived in this study). MODIS albedo is calculated from narrowband information and provided for different broadband regions of the spectrum (visible, near-infrared, shortwave, etc.) [see discussion in Houldcroft et al. (2009)]. Consequently, those albedos are not identical to the broadband albedo used by the Noah LSM (based on AVHRR), implying that the comparison is not straight, but still informative. [A method to convert MODIS albedo for use with the Noah LSM is discussed in Liang et al. (2005).]

Figure A1 presents the scatterplots at the four locations, where it can be noted that the EFT albedo

estimates (red circles) do not match the MODIS albedo, but they are closer to it than are the IGBP LC or MODIS LC albedo estimates (blue and black circles respectively). That is, they tend to have a better correspondence with observations than the other estimates. Time series for the whole period (not shown) confirm this assessment. The examples presented here are for selected locations, but no particular effort was done to choose them. They indicate that EFTs are a helpful approach to represent the geographical and temporal changes in the land surface biophysical properties.

Part of the reason for the improvement may be attributed to the fact that the conventional land-cover representation prescribes properties for each land cover regardless of whether it is a wet or dry year. The EFT approach is based on satellite-estimated exchanges of mass and energy between land and atmosphere regardless of the land-cover type, and therefore the biophysical properties will be sensitive to changes due to a wetter or drier year, even when land-cover categories are assumed to be the same.

REFERENCES

Aceituno, P., 1988: On the functioning of the Southern Oscillation in the South American sector. Part I: Surface climate. *Mon. Wea. Rev.,* **116,** 505–524, doi:10.1175/1520-0493(1988)116<0505:OTFOTS>2.0.CO;2.

Alcaraz-Segura, D., J. M. Paruelo, and J. Cabello, 2006: Identification of current ecosystem functional types in the Iberian Peninsula. *Global Ecol. Biogeogr.,* **15,** 200–212, doi:10.1111/j.1466-822X.2006.00215.x.

——, E. H. Berbery, S.-J. Lee, and J. M. Paruelo, 2011: Use of ecosystem functional types to represent the interannual variability of vegetation biophysical properties in regional models. *CLIVAR Exchanges,* No. 55, International CLIVAR Project Office, Southampton, United Kingdom, 23–27.

——, ——, O. Müller, and J. M. Paruelo, 2013a: Characterizing and monitoring climate regulation services. *Earth Observation of Ecosystem Services,* D. Alcaraz-Segura, C. M. Di Bella, and J. V. Straschnoy, Eds., CRC Press, 351–378.

——, J. M. Paruelo, H. E. Epstein, and J. Cabello, 2013b: Environmental and human controls of ecosystem functional diversity in temperate South America. *Remote Sens.,* **5,** 127–154, doi:10.3390/rs5010127.

Anderson, J. R., E. E. Hardy, J. T. Roach, and R. E. Witmer, 1976: A land use and land cover classification system for use with remote sensor data. U.S. Geological Survey Professional Paper 964, 28 pp.

Avila, F. B., A. J. Pitman, M. G. Donat, L. V. Alexander, and G. Abramowitz, 2012: Climate model simulated changes in temperature extremes due to land cover change. *J. Geophys. Res.,* **117,** D04108, doi:10.1029/2011JD016382.

Baidya Roy, S., and R. Avissar, 2002: Impact of land use/land cover change on regional hydrometeorology in Amazonia. *J. Geophys. Res.,* **107,** doi:10.1029/2000JD000266.

Beltrán-Przekurat, A., R. A. Pielke Sr., J. L. Eastman, and M. B. Coughenour, 2012: Modelling the effects of land-use/land-cover changes on the near-surface atmosphere in southern

South America. *Int. J. Climatol.,* **32,** 1206–1225, doi:10.1002/joc.2346.

Betts, A. K., J. H. Ball, A. C. M. Beljaars, M. J. Miller, and P. A. Viterbo, 1996: The land surface-atmosphere interaction: A review based on observational and modeling perspectives. *J. Geophys. Res.,* **101,** 7209–7225, doi:10.1029/95JD02135.

Bidegain, M., 2009: Severe drought in central Argentina and Uruguay [in "State of the Climate in 2008"]. *Bull. Amer. Meteor. Soc.,* **90** (8), S138.

Chen, F., and J. Dudhia, 2001: Coupling an advanced land surface–hydrology model with the Penn State–NCAR MM5 modeling system. Part I: Model implementation and sensitivity. *Mon. Wea. Rev.,* **129,** 569–585, doi:10.1175/1520-0493(2001)129<0569:CAALSH>2.0.CO;2.

——, K. Mitchell, and J. Schaake, 1996: Modeling of land surface evaporation by four schemes and comparison with FIFE observations. *J. Geophys. Res.,* **101,** 7251–7268, doi:10.1029/95JD02165.

Deo, R. C., J. I. Syktus, C. A. McAlpine, P. J. Lawrence, H. A. McGowan, and S. R. Phinn, 2009: Impact of historical land cover change on daily indices of climate extremes including droughts in eastern Australia. *Geophys. Res. Lett.,* **36,** L08705, doi:10.1029/2009GL037666.

Doyle, M. E., R. I. Saurral, and V. R. Barros, 2012: Trends in the distributions of aggregated monthly precipitation over the La Plata Basin. *Int. J. Climatol.,* **32,** 2149–2162, doi:10.1002/joc.2429.

Dros, J. M., 2004: Managing the soy boom: Two scenarios of soy production expansion in South America. AIDEnvironment Rep., 65 pp. [Available online at http://assets.panda.org/downloads/managingthesoyboomenglish_nbvt.pdf.]

Eidenshink, J. C., and J. L. Faudeen, 1994: The 1 km AVHRR global land data set: First stages in implementation. *Int. J. Remote Sens.,* **15,** 3443–3462, doi:10.1080/01431169408954339.

Ek, M. B., K. E. Mitchell, Y. Lin, E. Rogers, P. Grummann, V. Koren, G. Gayno, and J. D. Tarpley, 2003: Implementation of Noah land surface model advances in the National Centers for Environmental Prediction operational Mesoscale Eta Model. *J. Geophys. Res.,* **108,** 8851, doi:10.1029/2002JD003296.

Eltahir, E. A. B., 1998: A soil moisture-rainfall feedback mechanism. 1. Theory and observations. *Water Resour. Res.,* **34,** 765–776, doi:10.1029/97WR03499.

Entekhabi, D., I. Rodriguez-Iturbe, and R. L. Bras, 1992: Variability in large-scale water balance with land surface–atmosphere interaction. *J. Climate,* **5,** 798–813, doi:10.1175/1520-0442(1992)005<0798:VILSWB>2.0.CO;2.

Fan, Y., and H. Van den Dool, 2004: Climate Prediction Center global monthly soil moisture data set at 0.5° resolution for 1948 to present. *J. Geophys. Res.,* **109,** D10102, doi:10.1029/2003JD004345.

——, and ——, 2008: A global monthly land surface air temperature analysis for 1948-present. *J. Geophys. Res.,* **113,** D01103, doi:10.1029/2007JD008470.

Foley, J. A., S. Levis, M. H. Costa, W. Cramer, and D. Pollard, 2000: Incorporating dynamic vegetation cover within global climate models. *Ecol. Appl.,* **10,** 1620–1632, doi:10.1890/1051-0761(2000)010[1620:IDVCWG]2.0.CO;2.

Friedl, M. A., and Coauthors, 2002: Global land cover mapping from MODIS: Algorithms and early results. *Remote Sens. Environ.,* **83,** 287–302, doi:10.1016/S0034-4257(02)00078-0.

——, D. Sulla-Menashe, B. Tan, A. Schneider, N. Ramankutty, A. Sibley, and X. Huang, 2010: MODIS collection 5 global land cover: Algorithm refinements and characterization of new datasets. *Remote Sens. Environ.,* **114,** 168–182, doi:10.1016/j.rse.2009.08.016.

Ge, J., J. Qi, B. M. Lofgren, N. Moore, N. Torbick, and J. M. Olson, 2007: Impacts of land use/cover classification accuracy on regional climate simulations. *J. Geophys. Res.,* **112,** D05107, doi:10.1029/2006JD007404.

Guo, Z., P. A. Dirmeyer, and T. DelSole, 2011: Land surface impacts on subseasonal and seasonal predictability. *Geophys. Res. Lett.,* **38,** L24812, doi:10.1029/2011GL048611.

Hoffman, R. N., and E. Kalnay, 1983: Lagged average forecasting, an alternative to Monte Carlo forecasting. *Tellus,* **35A,** 100–118, doi:10.1111/j.1600-0870.1983.tb00189.x.

Hong, S.-Y., and E. Kalnay, 2002: The 1998 Oklahoma–Texas drought: Mechanistic experiments with NCEP global and regional models. *J. Climate,* **15,** 945–963, doi:10.1175/1520-0442(2002)015<0945:TOTDME>2.0.CO;2.

Houldcroft, C., W. M. F. Grey, M. Barnsley, C. M. Taylor, S. O. Los, and P. R. J. North, 2009: New vegetation albedo parameters and global fields of soil background albedo derived from MODIS for use in a climate model. *J. Hydrometeor.,* **10,** 183–198, doi:10.1175/2008JHM1021.1.

Huffman, G. J., R. F. Adler, D. T. Bolvin, G. Gu, E. J. Nelkin, K. P. Bowman, E. F. Stocker, and D. B. Wolff, 2007: The TRMM Multisatellite Precipitation Analysis (TMPA): Quasi-global, multiyear, combined-sensor precipitation estimates at fine scales. *J. Hydrometeor.,* **8,** 38–55, doi:10.1175/JHM560.1.

Izquierdo, A. E., C. D. De Angelo, and T. M. Aide, 2008: Thirty years of human demography and land-use change in the Atlantic Forest of Misiones, Argentina: An evaluation of the forest transition model. *Ecol. Soc.,* **13** (2), 3. [Available online at www.ecologyandsociety.org/vol13/iss2/art3/.]

Jiang, L., and Coauthors, 2010: Real-time weekly global green vegetation fraction derived from advanced very high resolution radiometer-based NOAA operational global vegetation index (GVI) system. *J. Geophys. Res.,* **115,** D11114, doi:10.1029/2009JD013204.

Kalnay, E., and Coauthors, 1996: The NCEP/NCAR 40-Year Reanalysis Project. *Bull. Amer. Meteor. Soc.,* **77,** 437–471, doi:10.1175/1520-0477(1996)077<0437:TNYRP>2.0.CO;2.

Kaufmann, R. K., L. Zhou, R. B. Myneni, J. Tucker, D. Slayback, N. V. Shabanov, and J. Pinzon, 2003: The effect of vegetation on surface temperature: A statistical analysis of NDVI and climate data. *Geophys. Res. Lett.,* **30,** 2147, doi:10.1029/2003GL018251.

Koster, R. D., and M. J. Suarez, 2003: Impact of land surface initialization on seasonal precipitation prediction and temperature prediction. *J. Hydrometeor.,* **4,** 408–423, doi:10.1175/1525-7541(2003)4<408:IOLSIO>2.0.CO;2.

——, ——, and M. Heiser, 2000: Variance and predictability of precipitation at seasonal-to-interannual timescales. *J. Hydrometeor.,* **1,** 26–46, doi:10.1175/1525-7541(2000)001<0026:VAPOPA>2.0.CO;2.

Krepper, C. M., and G. V. Zucarelli, 2009: Climatology of water excesses and shortages in the La Plata Basin. *Theor. Appl. Climatol.,* **102,** 13–27, doi:10.1007/s00704-009-0234-6.

Kurkowski, N. P., D. J. Stensrud, and M. E. Baldwin, 2003: Assessment of implementing satellite-derived land cover data in the Eta model. *Wea. Forecasting,* **18,** 404–416, doi:10.1175/1520-0434(2003)18<404:AOISDL>2.0.CO;2.

Lawrence, P. J., and T. N. Chase, 2007: Representing a new MODIS consistent land surface in the Community Land Model (CLM3.0). *J. Geophys. Res.,* **112,** G01023, doi:10.1029/2006JG000168.

Lee, S.-J., 2010: Impact of land surface vegetation change over the La Plata basin on the regional climatic environment: A study

using conventional land-cover/land-use and newly developed ecosystem functional types. Ph.D. dissertation, University of Maryland, 153 pp.

——, and E. H. Berbery, 2012: Land cover change effects on the climate of the La Plata basin. *J. Hydrometeor.,* **13,** 84–102, doi:10.1175/JHM-D-11-021.1.

——, ——, and D. Alcaraz-Segura, 2013a: Effects of implementing ecosystem functional type data in a mesoscale climate model. *Adv. Atmos. Sci.,* **30,** 1373–1386, doi:10.1007/s00376-012-2143-3.

——, ——, and ——, 2013b: The impact of ecosystem functional type changes on the climate of the La Plata basin. *Adv. Atmos. Sci.,* **30,** 1387–1405, doi:10.1007/s00376-012-2149-x.

Levis, S., G. B. Bonan, M. Vertenstein, and K. W. Oleson, 2004: The Community Land Model's Dynamic Global Vegetation Model (CLM-DGVM): Technical description and user's guide. NCAR Tech. Note TN-459+IA, 50 pp.

Liang, X.-Z., and Coauthors, 2005: Development of land surface albedo parameterization based on Moderate Resolution Imaging Spectroradiometer (MODIS) data. *J. Geophys. Res.,* **110,** D11107, doi:10.1029/2004JD005579.

Mahmood, R., and Coauthors, 2010: Impacts of land use/land cover change on climate and future research priorities. *Bull. Amer. Meteor. Soc.,* **91,** 37–46, doi:10.1175/2009BAMS2769.1.

McNaughton, S. J., M. Oesterheld, D. A. Frank, and K. J. Williams, 1989: Ecosystem-level patterns of primary productivity and herbivory in terrestrial habitats. *Nature,* **341,** 142–144, doi:10.1038/341142a0.

Mechoso, C. R., and G. Perez-Iribarren, 1992: Streamflow in southeastern South America and the Southern Oscillation. *J. Climate,* **5,** 1535–1539, doi:10.1175/1520-0442(1992)005<1535: SISSAA>2.0.CO;2.

Miller, J., M. Barlage, X. Zeng, H. Wei, K. Mitchell, and D. Tarpley, 2006: Sensitivity of the NCEP/Noah land surface model to the MODIS green vegetation fraction data set. *Geophys. Res. Lett.,* **33,** L13404, doi:10.1029/2006GL026636.

Mo, K. C., 2008: Model-based drought indices over the United States. *J. Hydrometeor.,* **9,** 1212–1230, doi:10.1175/2008JHM1002.1.

——, and E. H. Berbery, 2011: Drought and persistent wet spells over South America based on observations and the U.S. CLIVAR drought experiments. *J. Climate,* **24,** 1801–1820, doi:10.1175/2010JCLI3874.1.

Niu, G.-Y., and Coauthors, 2011: The community Noah land surface model with multiparameterization options (Noah-MP): 1. Model description and evaluation with local-scale measurements. *J. Geophys. Res.,* **116,** D12109, doi:10.1029/2010JD015139.

Paruelo, J. M., E. G. Jobbágy, and O. E. Sala, 2001: Current distribution of ecosystem functional types in temperate South America. *Ecosystems,* **4,** 683–698, doi:10.1007/s10021-001-0037-9.

——, J. P. Guerschman, and S. R. Verón, 2005: Expansión agrícola y cambios en el uso del suelo. *Cienc. Hoy,* **15** (87), 14–23.

Penalba, O., J. Rivera, and M. L. Bettolli, 2010: Trends and periodicities in the annual amount of dry days over Argentina, looking towards the climatic change. *Options Méditerr.,* **95A,** 27–33.

Pielke, R. A., J. Adegoke, A. Beltrán-Przekurat, C. A. Hiemstra, J. Lin, U. S. Nair, D. Niyogi, and T. E. Nobis, 2007: An overview of regional land-use and land-cover impacts on rainfall. *Tellus,* **59B,** 587–601, doi:10.1111/j.1600-0889.2007.00251.x.

Ropelewski, C. F., and M. S. Halpert, 1987: Global and regional scale precipitation patterns associated with the El Niño/Southern Oscillation. *Mon. Wea. Rev.,* **115,** 1606–1626, doi:10.1175/1520-0493(1987)115<1606: GARSPP>2.0.CO;2.

Rusticucci, M., J. Marengo, O. Penalba, and M. Renom, 2010: An intercomparison of model-simulated in extreme rainfall and temperature events during the last half of the twentieth century. Part 1: Mean values and variability. *Climate Dyn.,* **98,** 493–508, doi:10.1007/s10584-009-9742-8.

Seager, R., N. Naik, W. Baethgen, A. Robertson, Y. Kushnir, J. Nakamura, and S. Jurburg, 2010: Tropical oceanic causes of interannual to multidecadal precipitation variability in southeast South America over the past century. *J. Climate,* **23,** 5517–5539, doi:10.1175/2010JCLI3578.1.

Sellers, P. J., M. D. Heiser, and F. G. Hall, 1992: Relations between surface conductance and spectral vegetation indices at intermediate (100 m^2 to 15 km^2) length scales. *J. Geophys. Res.,* **97,** 19 033–19 059, doi:10.1029/92JD01096.

Seneviratne, S. I., T. Corti, E. L. Davin, M. Hirschi, E. B. Jaeger, I. Lehner, B. Orlowsky, and A. J. Teuling, 2010: Investigating soil moisture climate interactions in a changing climate: A review. *Earth-Sci. Rev.,* **99,** 125–161, doi:10.1016/j.earscirev.2010.02.004.

Shi, W., R. W. Higgins, E. Yarosh, and V. E. Kousky, 2000: *The Annual Cycle and Variability of Precipitation in Brazil.* NCEP/Climate Prediction Center Atlas 9, 25 pp. [Available online at http://www.cpc.ncep.noaa.gov/products/outreach/research_papers/ncep_cpc_atlas/9/.]

Silva, V. B. S., V. E. Kousky, W. Shi, and R. W. Higgins, 2007: An improved gridded historical daily precipitation analysis for Brazil. *J. Hydrometeor.,* **8,** 847–861, doi:10.1175/JHM598.1.

Silvestri, G., and C. Vera 2008: Evaluation of the WCRP-CMIP3 model simulations in the La Plata basin. *Meteor. Appl.,* **15,** 497–502, doi:10.1002/met.98.

Skamarock, W. C., and Coauthors, 2008: A description of the Advanced Research WRF version 3. NCAR Tech. Note NCAR/TN-4751+STR, 125 pp.

Smith, B., I. C. Prentice, and M. T. Sykes, 2001: Representation of vegetation dynamics in modelling of terrestrial ecosystems: Comparing two contrasting approaches within European climate space. *Global Ecol. Biogeogr.,* **10,** 621–637, doi:10.1046/j.1466-822X.2001.00256.x.

Solman, S. A., M. N. Núñez, and M. F. Cabré, 2008: Regional climate change experiments over southern South America. I: Present climate. *Climate Dyn.,* **30,** 533–552, doi:10.1007/s00382-007-0304-3.

Tian, Y., R. E. Dickinson, L. Zhou, R. B. Myneni, M. Friedl, C. B. Schaaf, M. Carroll, and F. Gao, 2004a: Land boundary conditions from MODIS data and consequences for the albedo of a climate model. *Geophys. Res. Lett.,* **31,** L05504, doi:10.1029/2003GL019104.

——, ——, ——, and M. Shaikh, 2004b: Impact of new land boundary conditions from Moderate Resolution Imaging Spectroradiometer (MODIS) data on the climatology of land surface variables. *J. Geophys. Res.,* **109,** D20115, doi:10.1029/2003JD004499.

Valentini, R., D. D. Baldocchi, J. D. Tenhunen, and P. Kabat, 1999: Ecological controls on land-surface atmospheric interactions. *Integrating Hydrology, Ecosystem Dynamics, and Biogeochemistry in Complex Landscapes,* J. D. Tenhunen and P. Kabat, Eds., John Wiley & Sons, 105–116.

Volante, J. N., D. Alcaraz-Segura, M. J. Mosciaro, E. F. Viglizzo, and J. M. Paruelo, 2012: Ecosystem functional changes

associated with land clearing in NW Argentina. *Agric. Ecosyst. Environ.,* **154,** 12–22, doi:10.1016/j.agee.2011.08.012.

Weiss, M., B. van den Hurk, R. Haarsma, and W. Hazeleger, 2012: Impact of vegetation variability on potential predictability and skill of EC-Earth simulations. *Climate Dyn.,* **39,** 2733–2746, doi:10.1007/s00382-012-1572-0.

Xue, Y., F. J. Zeng, K. E. Mitchell, Z. Janjić, and E. Rogers, 2001: The impact of land surface processes on simulations of the U.S. hydrological cycle: A case study of the 1993 flood using the SSiB land surface model in the NCEP Eta regional model. *Mon. Wea. Rev.,* **129,** 2833–2860, doi:10.1175/1520-0493(2001)129<2833:TIOLSP>2.0.CO;2.

Zeng, X.-M., Z.-H. Wu, S. Song, S.-Y. Xiong, Y.-Q. Zheng, Z.-G. Zhou, and H.-Q. Liu, 2012: Effects of different land-surface schemes on the simulation of a heavy rainfall event by WRF. *Chin. J. Geophys.,* **55,** 394–408, doi:10.1002/cjg2.1734.

CORRIGENDUM

OMAR V. MÜLLER

*CEVARCAM, Facultad de Ingeniería y Ciencias Hídricas, Universidad Nacional del Litoral and CONICET,
Santa Fe, Argentina*

ERNESTO HUGO BERBERY

*Cooperative Institute for Climate and Satellites-Maryland, Earth System Science Interdisciplinary Center,
University of Maryland, College Park, College Park, Maryland*

DOMINGO ALCARAZ-SEGURA

Departamento de Botánica, Campus de Fuente Nueva, Universidad de Granada, Granada, Spain

MICHAEL B. EK

Environmental Modeling Center, NOAA/NCEP/NWS, College Park, Maryland

(Manuscript received and in final form 30 June 2015)

An incorrect version of Fig. 13a was published in Müller et al. (2014). Figure 13a on page 6771 did not show the gray band representing the eastern region area-averaged 2-m temperature for CPC and OBS (Climate Prediction Center and Observations). The correct figure is provided here. We regret any inconvenience.

REFERENCE

Müller, O. V., E. H. Berbery, D. Alcaraz-Segura, and M. B. Ek, 2014: Regional model simulations of the 2008 drought in southern South America using a consistent set of land surface properties. *J. Climate*, **27**, 6754–6778, doi:10.1175/JCLI-D-13-00463.1.
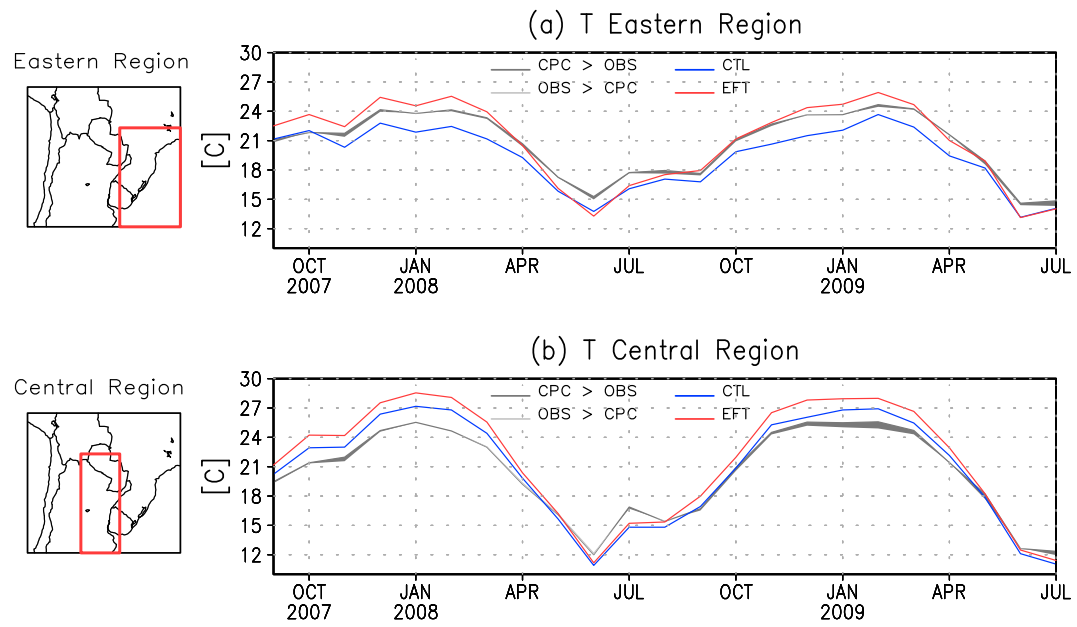
FIG. 13. Area-averaged 2-m temperature for CPC and OBS (their slight differences are shaded) CTL and EFT over two regions denoted to the left: (a) eastern region and (b) central region. Only data over land were considered.